

Using galaxy-galaxy weak lensing measurements to correct the Finger-of-God

Chiaki Hikage^{1,2}, Masahiro Takada³, David N. Spergel^{1,3}

¹ *Department of Astrophysical Sciences, Princeton University, Peyton Hall, Princeton NJ 08544, USA*

² *Kobayashi-Maskawa Institute for the Origin of Particles and the Universe (KMI), Nagoya University, Aichi 464-8602, Japan*

³ *Institute for the Physics and Mathematics of the Universe (IPMU), The University of Tokyo, Chiba 277-8582, Japan*

28 October 2018

ABSTRACT

For decades, cosmologists have been using galaxies to trace the large-scale distribution of matter. At present, the largest source of systematic uncertainty in this analysis is the challenge of modeling the complex relationship between galaxy redshift and the distribution of dark matter. If all galaxies sat in the centers of halos, there would be minimal Finger-of-God (FoG) effects and a simple relationship between the galaxy and matter distributions. However, many galaxies, even some of the luminous red galaxies (LRGs), do not lie in the centers of halos. Because the galaxy-galaxy lensing is also sensitive to the off-centered galaxies, we show that we can use the lensing measurements to determine the amplitude of this effect and to determine the expected amplitude of FoG effects. We develop an approach for using the lensing data to model how the FoG suppresses the power spectrum amplitudes and show that the current data implies a 30% suppression at wavenumber $k = 0.2 \text{ hMpc}^{-1}$. Our analysis implies that it is important to complement a spectroscopic survey with an imaging survey with sufficient depth and wide field coverage. Joint imaging and spectroscopic surveys allow a robust, unbiased use of the power spectrum amplitude information: it improves the marginalized error of growth rate $f_g \equiv d \ln D / d \ln a$ by up to a factor of 2 over a wide range of redshifts $z < 1.4$. We also find that the dark energy equation-of-state parameter, w_0 , and the neutrino mass, f_ν , can be unbiasedly constrained by combining the lensing information, with an improvement of 10–25% compared to a spectroscopic survey without lensing calibration.

Key words: cosmology: theory – galaxy clustering – dark energy

1 INTRODUCTION

Over the past three decades, astronomers have been conducting ever larger redshift surveys in their efforts to probe the large-scale structure of the universe (Davis & Huchra 1982; de Lapparent et al. 1986; Kirshner et al. 1987; York et al. 2000; Peacock et al. 2001). In the coming decade, we are embarking on even larger surveys: BOSS¹, WiggleZ² (Blake et al. 2011), Vipers³, FMOS⁴, HETDEX⁵, BigBOSS⁶ (Schlegel et al. 2009), LAMOST⁷, Subaru PFS⁸, Euclid⁹, and WFIRST¹⁰. This upcoming generation of surveys are motivated by our desire to understand cosmic acceleration and to measure the composition of the universe by simultaneously measuring geometry and dynamics. The combination of cosmic microwave background (CMB) data and large redshift surveys trace the growth of structure formation from the last-scattering surface ($z \simeq 1100$) to low redshifts and determine cosmological parameters to high precision (Wang et al. 1999; Eisenstein et al.

¹ <http://cosmology.lbl.gov/BOSS/>

² <http://wigglez.swin.edu.au/site/>

³ <http://vipers.inaf.it/>

⁴ <http://www.naoj.org/Observing/Instruments/FMOS/>

⁵ <http://hetdex.org/>

⁶ <http://bigboss.lbl.gov/>

⁷ <http://www.lamost.org/website/en>

⁸ <http://sumire.ipmu.jp/en/>

⁹ <http://sci.esa.int/euclid>

¹⁰ <http://wfirst.gsfc.nasa.gov/>

1999; Tegmark et al. 2004; Cole et al. 2005). Measurements of the baryon acoustic oscillation (BAO) scale provide us with a robust geometrical probe of the angular diameter distance and the Hubble expansion rate (Eisenstein et al. 2005; Percival et al. 2007). Observations of redshift-space distortion measure the growth rate of structure formation (Zhang et al. 2007; Guzzo et al. 2008; Wang 2008; Guzik et al. 2010; White et al. 2009; Percival & White 2009; Song & Percival 2009; Song & Kayo 2010; Yamamoto et al. 2010; Tang et al. 2011). Combining measurements of the growth of structure formation and the geometry of the universe provides a key clue to understanding the nature of dark energy, properties of gravity on cosmological scales, or the nature of cosmic acceleration (Albrecht et al. 2006; Peacock et al. 2006).

The galaxy power spectrum in redshift space, a direct observable from a redshift survey, is a two-dimensional function of wavelengths perpendicular and parallel to the line-of-sight direction (Peacock et al. 2001; Okumura et al. 2008; Guzzo et al. 2008). While galaxy clustering in real space is statistically isotropic in an isotropic and homogeneous universe, the line-of-sight components of galaxies' peculiar velocities alter galaxy clustering in redshift space (Kaiser 1987). For review, see Hamilton (1998). The amplitude of the distortion depends both on geometry and dynamics (Alcock & Paczynski 1979; Seo & Eisenstein 2003).

For the surveys to achieve their ambitious goals for precision cosmology, we will need a detailed understanding of the underlying systematics. One of the major systematic uncertainties in redshift-space power spectrum measurements is non-linear redshift distortion due to the internal motion of galaxies within halos, the so-called Finger-of-God (FoG) effect (Jackson 1972; Scoccimarro 2004). Since it is sensitive to highly non-linear physics as well as difficult to model galaxy formation/assembly histories, the FoG effect is the dominant systematic in redshift surveys.

Reid et al. (2009) advocated using halos rather than Luminous Red Galaxies (LRGs; Eisenstein et al. 2001) to trace large-scale structure. In an analysis of LRGs sampled with the Sloan Digital Sky Survey (SDSS)¹¹, Reid et al. (2010) implemented this scheme by removing satellite LRGs from the same halo with the aid of the mock catalog and the halo model prescription. From the SDSS LRG dataset, Reid et al. (2010) found that about 6% of LRGs are satellite galaxies, while the remaining 94% are central galaxies of halos with masses $\gtrsim 10^{13} M_{\odot}$. Once such a halo catalog is constructed, clustering properties of halos are easier to model, because halos have only bulk motions in large-scale structure, and therefore have the reduced FoG effect. Despite this effort, the remaining FoG effect is a dominant systematic uncertainty.

FoG effects are just one of the non-linear systematics. Future analysis of the redshift-space power spectrum of halos will need to model non-linear clustering, non-linear bias, and non-linear redshift distortion effect due to their bulk motions. Recent simulations and refined perturbation theory suggest that halo clustering based approach seems a very promising probe of cosmology (Scoccimarro 2004; Crocce & Scoccimarro 2006; Matsubara 2008; Saito et al. 2011; Taruya et al. 2010; Tang et al. 2011; Reid & White 2011; Sato & Matsubara 2011).

For a halo-based catalog, a significant source of uncertainty is the position of the galaxies in the halos. Ho et al. (2009) compared LRG positions with the X-ray surface-brightness peak, reporting a sizable positional difference. For the LRG analysis, this is the dominant uncertainty (see Reid et al. 2010, for the useful discussion in Appendix C). The virial theorem implies that off-centered LRGs are moving relative to the halo center thus producing an FoG effect.

In this paper, we propose a novel method of using a cross-correlation of spectroscopic galaxies (e.g., LRGs) with background galaxy images to correct the FoG contamination to the redshift-space power spectrum. Dark matter halos hosting spectroscopic galaxies induce a coherent lensing distortion effect on background galaxy images, and the signals are measurable using the cross-correlation method – the so-called galaxy-galaxy or cluster-galaxy weak lensing. The lensing signals have been now measured at a high significance by various groups (Mandelbaum et al. 2006; Sheldon et al. 2009; Leauthaud et al. 2010; Okabe et al. 2010). If we include off-centered galaxies and use the galaxy position as a halo center proxy of each halo in the lensing analysis, the lensing signals at angular scales smaller than the typical offset scale are diluted (see Oguri & Takada 2011, for a useful formulation of the off-centering effect on cluster-galaxy weak lensing). Thus the galaxy-galaxy lensing signals can be used to infer the amount of the off-centered galaxy contamination (Johnston et al. 2007; Leauthaud et al. 2010; Okabe et al. 2010). Furthermore, since lensing is a unique means of reconstructing the dark matter distribution, it may allow us to infer the halo center on individual halo basis if a sufficiently high signal-to-noise ratio is available (Oguri et al. 2010). Hence, a weak-lensing based calibration of the FoG effect in redshift-space power spectrum measurements may be feasible if spectroscopic and imaging surveys observe the same region of the sky. Fortunately, many upcoming surveys will survey the same region of the sky: the BOSS and Subaru Hyper SuprimeCam (HSC) Survey (Miyazaki et al. 2006), the Subaru PFS and HSC surveys (Subaru Measurements of Images and Redshifts: the SuMIRE project), Euclid and WFIRST or a combination of LSST (LSST Science Collaborations et al. 2009) with spectroscopic surveys.

In Section 2, we will first develop a model of computing the redshift-space power spectrum of LRGs based on the halo model approach (see Cooray & Sheth 2002, for a thorough review). Extending White (2001) and Seljak (2001), we model the distribution of off-centered LRGs as a source of FoG distortions. Following the method in Oguri & Takada (2011), we also model the distribution of off-centered LRGs as a source of smoothing of the LRG-galaxy lensing signal. Assuming survey parameters of the Subaru HSC imaging survey combined with the BOSS and/or Subaru PFS spectroscopic surveys as well as the Euclid imaging and spectroscopic surveys, we study the impact of the FoG effect on parameter estimations. We also study the ability of the combined imaging and spectroscopic surveys for correcting for the FoG effect contamination based on the off-centering information inferred from the LRG-galaxy lensing measurements. For the parameter forecast, we pay particular attention to the dark energy equation-of-state parameter, w_0 , the neutrino mass parameter, f_{ν} , and the growth rate at each redshift slice. Unless explicitly stated we will throughout this paper assume a WMAP-normalized Λ CDM model as our fiducial

¹¹ <http://www.sdss.org/>

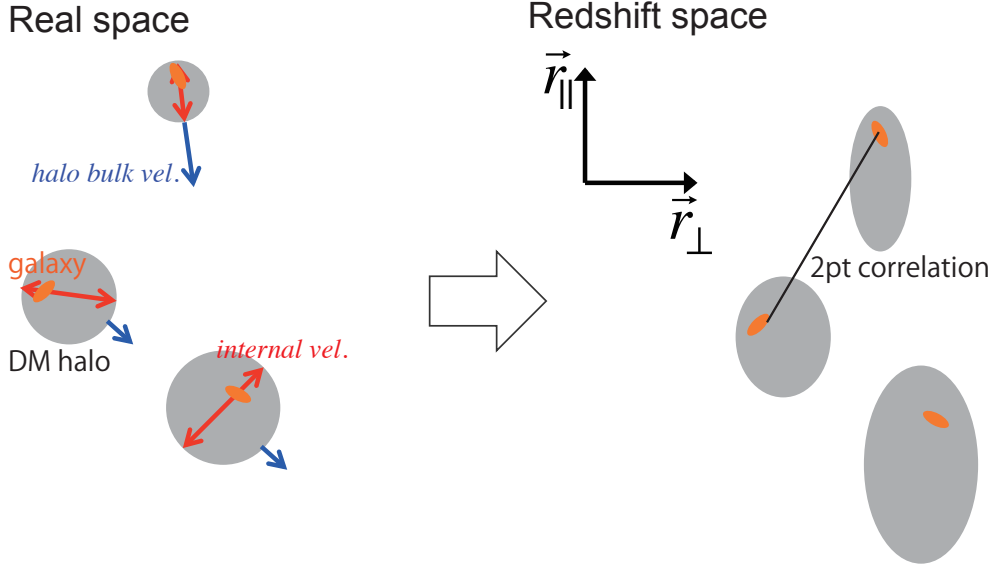


Figure 1. A schematic illustration of the redshift-distortion effect on redshift-space clustering of dominant luminous red galaxies (DLRGs; see text for details). We assume that a catalog of DLRGs is constructed so that each halo contains one DLRG. The redshift distortion effect on the redshift-space power spectrum of DLRGs arises from two contributions: the bulk motion of halos that host each DLRG, and the internal motion of DLRG within a halo, the Finger-of-God (FoG) effect. If some of the LRGs are not in the center of their halos, then their motions produce significant FoG effects. The halo bulk motion causes a displacement of halo position in redshift space, while the internal motion stretches the distribution region of DLRGs within a halo along the line-of-sight direction.

cosmological model (Komatsu et al. 2009): $\Omega_b h^2 = 0.0226$, $\Omega_{\text{cdm}} h^2 = 0.1109$, $\Omega_\Lambda = 0.734$, respectively, $\tau = 0.088$, $n_s = 0.963$, $A(k = 0.002 \text{Mpc}^{-1}) = 2.43 \times 10^{-9}$, where Ω_b , Ω_{cdm} and Ω_Λ are the energy density parameters of baryon, CDM and dark energy (the cosmological constant with $w_0 = -1$ here), τ is the optical depth to the last scattering surface, and n_s and A are the tilt and amplitude of the primordial curvature power spectrum.

2 FORMULATION: REDSHIFT-SPACE POWER SPECTRUM

In this section, we give a formulation for modeling the redshift-space power spectrum of luminous red galaxies (LRGs) based on the halo model approach (White 2001; Seljak 2001).

2.1 Dominant Luminous Red Galaxies (DLRGs)

Weak lensing studies (Mandelbaum et al. 2006; Johnston et al. 2007) and clustering analyses (Ross et al. 2007, 2008; Wake et al. 2008; Zheng et al. 2009; Reid & Spergel 2009; White et al. 2011) find that most LRGs reside in massive halos. While the typical massive halo contains only one LRG, roughly 5-10% of all LRGs are satellite galaxies in a halo containing multiple LRGs. These satellite galaxies contribute a large one halo term that is an additional source of shot noise and non-linearity in power spectrum estimation. Reid et al. (2009) outline a procedure of identifying these satellite LRGs through finding multiple pairs that lie in common halos (or the small spatial region) and then using only the brightest luminous red galaxies in each halo as a tracer. We call these galaxies dominant luminous red galaxies (DLRGs). These DLRGs are more linear tracers of the underlying matter field than the LRGs are. Reid et al. (2010) and Percival et al. (2010) adopt this procedure to determine the SDSS LRG power spectrum. In this paper, we focus on these DLRGs so that each halo contains either zero or one DLRG.

2.2 Halo Model Approach for DLRGs

Since there is only one DLRG per halo, the two-halo term determines the clustering of these galaxies in the halo model picture (Cooray & Sheth 2002; Takada & Jain 2003). If the DLRGs sat in the center of each halo, then the DLRG power spectrum would be linearly related to the halo power spectrum. However, since the DLRGs do not always lie in the center of the halo, the power spectrum is given as

$$P_{\text{DLRG}}(k) = \frac{1}{\bar{n}_{\text{DLRG}}^2} \int dM \int dM' \frac{dn}{dM} N_{\text{HOD}}(M) \tilde{p}_{\text{off}}(k; M) \frac{dn}{dM'} N_{\text{HOD}}(M') \tilde{p}_{\text{off}}(k; M') P_{\text{hh}}(k; M, M'), \quad (1)$$

where dn/dM is the halo mass function, $N_{\text{HOD}}(M)$ is the halo occupation number (note $N_{\text{HOD}} \leq 1$ as described below), and $P_{\text{hh}}(k; M, M')$ is the cross-power spectrum of halos of masses M and M' . Numerical simulations show that the halo cross-power spectrum is approximately

a linearly biased version of the matter power spectrum (Reid et al. 2009): $P_{\text{hh}}(k; M, M') \simeq b(M)b(M')P_{\text{m}}^{\text{NL}}(k)$, where $b(M)$ is the halo bias, and $P_{\text{m}}^{\text{NL}}(k)$ is the non-linear matter power spectrum. This approximation simplifies the relationship between the DLRG and matter power spectrum:

$$P_{\text{DLRG}}(k) = \left[\frac{1}{\bar{n}_{\text{DLRG}}} \int dM \frac{dn}{dM} b(M) N_{\text{HOD}}(M) \tilde{p}_{\text{off}}(k; M) \right]^2 P_{\text{m}}^{\text{NL}}(k). \quad (2)$$

The quantity \bar{n}_{DLRG} is the mean number density of DLRGs defined as

$$\bar{n}_{\text{DLRG}} \equiv \int dM \frac{dn}{dM} N_{\text{HOD}}(M). \quad (3)$$

The mean bias of halos hosting DLRGs is defined as

$$\bar{b} \equiv \frac{1}{\bar{n}_{\text{DLRG}}} \int dM b(M) \frac{dn}{dM} N_{\text{HOD}}(M). \quad (4)$$

The mean mass of halos hosting DLRGs is similarly estimated as $\bar{M}_h \equiv (1/\bar{n}_{\text{DLRG}}) \int dM M (dn/dM) N_{\text{HOD}}(M)$.

The coefficient $\tilde{p}_{\text{off}}(k; M)$ in Eq. (2) is the Fourier transform of the average radial profile of DLRGs within a halo with mass M :

$$\tilde{p}_{\text{off}}(k; M) = 4\pi \int_0^{r_{\text{vir}}} r^2 dr p_{\text{off}}(r) \frac{\sin(kr)}{kr}, \quad (5)$$

where $p_{\text{off}}(r)$ is normalized so as to satisfy $\int_0^{r_{\text{vir}}} 4\pi r^2 dr p_{\text{off}}(r) = 1$, and r_{vir} is the virial radius of a halo with mass M , which can be defined once the virial overdensity and the background cosmology are specified. Note that, since the power spectrum is a statistical quantity, we just need the averaged DLRG distribution within a halo, which is therefore a one-dimensional function of radius r with respect to the halo center in a statistically homogeneous and isotropic universe. In the following, quantities with tilde symbol denote their Fourier-transformed coefficients for our notational convention.

The term in the square bracket in Eq. (2) describes the halo exclusion effect. Because halos have finite sizes, roughly their virial radius, there is only one dominant galaxy in this region (see Fig. 1). If we are implementing an algorithm that eliminates multiple galaxies in the finite region, then we impose an exclusion region around each galaxy. The two halo term describes the correlations between two DLRGs in *two* different halos. The DLRG power spectrum at small scales (large k 's) is thus suppressed compared to the matter power spectrum multiplied with \bar{b}^2 (see Fig. 11 in Cooray & Sheth 2002).

If each DLRG resides at the center of each halo (e.g., the center of mass), $\tilde{p}_{\text{off}}(k) = 1$ (or $p_{\text{off}} \propto \delta_D(r)$). However some fraction of DLRGs in the sample are expected to have an offset from the halo center (Skibba et al. 2011). Due to the collision-less nature of dark matter, dark matter halos lack clear boundary with surrounding structures and do not have a spherically symmetric mass distribution. Thus the halo center is not a well-defined quantity. While DLRGs, the most massive galaxy in the halo, will eventually sink toward the center of the halo through dynamical friction, many clusters are dynamically young and have experienced recent interactions. Thus, we expect that DLRGs are not all in the centers of halos and that the distribution of their positions in the halos evolve with redshift.

How does this halo model picture need to be changed in redshift space? To model the redshift-space power spectrum, we need to properly take into account the redshift distortion effect due to peculiar velocities of DLRGs. If all DLRGs are located at the center in their host halos, DLRGs move together with their host halos having coherent, bulk velocities in large-scale structure, and the redshift-space clustering is not affected by the FoG effect. However, as illustrated in Fig. 1, if some DLRGs are offset from the center, they will have internal motions within their host halos, which causes the FoG effect. The virial theorem implies that the amplitude of the displacement of the DLRG from the center of its halo is directly related to the DLRG velocity dispersion within the halo.

In the halo model picture, the FoG effect can be incorporated by stretching the average radial profile of DLRGs along the line-of-sight direction by the amount of the internal motion, as illustrated in the right panel of Fig. 1. This stretch enhances the halo exclusion effect, which suppresses the power spectrum amplitudes. Thus the redshift-space distribution of DLRGs within a halo becomes two-dimensional, given as a function of two radii, r_{\perp} and r_{\parallel} , perpendicular and parallel to the line-of-sight direction with respect to the halo center. Also note that the internal velocity distribution of DLRGs within a halo is considered to be statistically isotropic and therefore it depends on the radius r from the halo center, halo mass M and redshift z (see Section 2.3.3 for details). The averaged redshift-space distribution of DLRGs within a halo, denoted as $p_{s,\text{off}}(r_{\perp}, r_{\parallel}; M)$, can be given as a smearing of the real-space distribution with the displacement function:

$$p_{s,\text{off}}(r_{\perp}, r_{\parallel}; M) = \int_{-\infty}^{\infty} dr'_{\parallel} R(r_{\parallel} - r'_{\parallel}; r', M) p_{\text{off}}\left(\sqrt{r_{\perp}^2 + r'_{\parallel}{}^2}\right), \quad (6)$$

where $R(\Delta r_{\parallel}; r, M)$ is the displacement function of DLRGs due to the velocity distribution inside a halo and satisfies the normalization condition: $\int d(\Delta r_{\parallel}) R(\Delta r_{\parallel}) = 1$. Assuming that the internal motion of DLRGs is much smaller than the speed of light, the displacement of the radial position of a given DLRG is directly related to the line-of-sight component of the internal velocity v_{\parallel} as

$$\Delta r_{\parallel} = \frac{v_{\parallel}}{aH(z)}, \quad (7)$$

where $H(z)$ is the Hubble expansion rate at the redshift of DLRG.

Hence, assuming a distant observer approximation, the redshift-space power spectrum of DLRGs can be given in terms of the Fourier-transform of $p_{s,\text{off}}(r_{\perp}, r_{\parallel}; M)$ as

$$P_{s,\text{DLRG}}(k, \mu) = \left[\frac{1}{\bar{n}_{\text{DLRG}}} \int dM \frac{dn}{dM} b(M) N_{\text{HOD}}(M) \tilde{p}_{s,\text{off}}(k, \mu; M) \right]^2 P_{s,m}^{\text{NL}}(k, \mu), \quad (8)$$

where μ is the cosine angle between the line-of-sight direction and the wavevector \mathbf{k} , i.e. $\mu \equiv k_{\parallel}/k$, and $P_{s,m}^{\text{NL}}(k_{\perp}, k_{\parallel})$ is the non-linear redshift-space power spectrum. In this paper, we simply assume that the redshift distortion effect due to the coherent bulk motion of halos is described by linear theory (Kaiser 1987):

$$P_{s,m}^{\text{NL}}(k, \mu) = P_m^{\text{NL}}(k) [1 + 2\beta\mu^2 + \beta^2\mu^4], \quad (9)$$

where $\beta \equiv f_g/\bar{b}$, f_g is the linear growth rate, $f_g \equiv d \ln D / d \ln a$, and \bar{b} is the effective bias of halos hosting the DLRGs (Eq. [4]). As given by the term in the square bracket in Eq. (8), the FoG effect due to off-centered DLRGs causes scale-dependent, angular anisotropies in the redshift power spectrum amplitudes.

In the limit that all DLRGs are at the true center of each halo, the redshift-space power spectrum (Eq. [8]) is reduced to the halo power spectrum in redshift space:

$$p_{\text{off}}(r) = \frac{1}{4\pi r^2} \delta_D(r) \rightarrow P_{s,\text{DLRG}}(k, \mu) = \bar{b}^2 P_{s,m}^{\text{NL}}(k, \mu) \simeq P_{s,\text{halo}}(k, \mu), \quad (10)$$

where $P_{s,\text{halo}}(k, \mu)$ is the halo power spectrum in redshift space. More rigorously speaking, halo clustering is affected by non-linearities in gravitational clustering, redshift distortion and biasing at scales even in the weakly non-linear regime we are interested in (Scoccimarro 2004; Taruya et al. 2009, 2010; Saito et al. 2011; Tang et al. 2011; Reid & White 2011; Sato & Matsubara 2011). For these we can use an accurate model of the redshift-space spectrum of halos by using refined perturbation theory and/or N-body and mock simulations (Taruya et al. 2009, 2010; Sato & Matsubara 2011). Hence we can extend the formulation above in order to include these non-linear effects, simply by using a model of non-linear, redshift-space halo power spectrum for $P_{s,\text{hh}}(k, \mu; M, M')$, instead of $b(M)b(M')P_{s,m}^{\text{NL}}(k, \mu)$ in Eq. (8). However, this is beyond the scope of this paper, and we here focus on the FoG effect by assuming the Kaiser formula (9) for the sake of clarity of our discussion.

2.3 Model ingredients

To compute the redshift-space power spectrum (Eq. [8]), we need to specify the model ingredients: halo occupation distribution of DLRGs, the off-centered distribution of DLRGs and the velocity distribution inside halos. In this subsection, we will give these model ingredients adopted in this paper.

2.3.1 HOD and the halo model ingredients

First we need to specify the halo mass function and the halo bias. We use the fitting formula developed in Sheth & Tormen (1999) to compute the halo mass function and the halo bias in our fiducial cosmological model (also see Takada & Jain 2003).

A useful, empirical method for describing clustering properties of galaxies is the halo occupation distribution (HOD) (Scoccimarro et al. 2001; Zheng et al. 2005, also see references therein). The HOD gives the average number of galaxies residing in halos of mass M and at redshift z . The previous works have shown that the halo model prediction using the HOD modeling can well reproduce the observed properties of LRG clustering over wide ranges of length scales and redshifts ($0 \lesssim z \lesssim 0.5$) (Zheng et al. 2009; Reid & Spergel 2009; White et al. 2011). Since we assume that satellite LRGs can be removed based on the method of Reid et al. (2010), we use the HOD for central LRGs that is found in Reid & Spergel (2009):

$$N_{\text{HOD}}(M) \simeq N_{\text{cen}}(M) = \frac{1}{2} \left[1 + \text{erf} \left(\frac{\log_{10}(M) - \log_{10}(M_{\text{min}})}{\sigma_{\log M}} \right) \right], \quad (11)$$

where $\text{erf}(x)$ is the error function, and we adopt $M_{\text{min}} = 8.05 \times 10^{13} M_{\odot}$ and $\sigma_{\log M} = 0.7$. We do not consider a possible redshift evolution of the HOD, because any strong redshift dependence has not been found from actual data. Note $N_{\text{HOD}}(M) \leq 1$. Also note that we use the HOD model for “central” galaxies, but this does not mean that all DLRGs under consideration are central galaxies, but each halo has *one* DLRG at most.

2.3.2 Radial profile of DLRGs

The radial profile of DLRGs is not well known, as the true center of a halo is not easy to estimate observationally. Several studies, both observational and numerical, suggest that the DLRG are more centrally concentrated than the dark matter, but do not all lie in the bottom of the dark matter potentials (Lin & Mohr 2004; Koester et al. 2007; Johnston et al. 2007; Ho et al. 2009; Hilbert & White 2010; Okabe et al. 2010; Oguri et al. 2010; Skibba et al. 2011). Ho et al. (2009) compared the LRG positions with X-ray peak positions for known X-ray

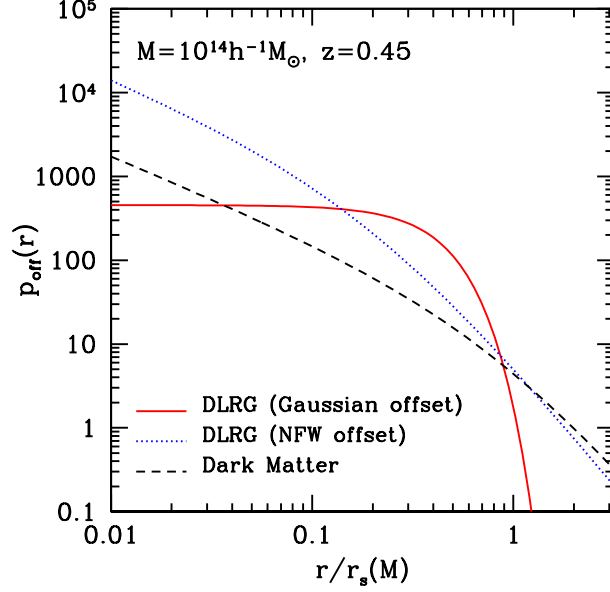


Figure 2. This figure shows the statistically averaged radial profile of dark matter and DLRGs in halos with mass $M = 10^{14} h^{-1} M_{\odot}$ and halo concentration $c_{\text{vir}} = 4.3$, and at redshift $z = 0.45$. The solid curve denotes a Gaussian radial profile (or off-centered) model with the width that is taken to be $r_{\text{off}} = 0.3r_s$ (~ 100 kpc), where r_s is the scale radius of the dark matter NFW profile. The dotted curve is an NFW radial profile model, which is given by the concentration parameter of $c_{\text{off}} = 20$.

clusters, and found that the LRG radial distribution can be fitted with an NFW profile with high concentration parameter ($c \sim 20$). Using the Subaru weak lensing observations for about 20 X-ray luminous clusters, Oguri et al. (2010) fit an elliptical NFW model to the dark matter distribution. They found that, for most clusters, the positional difference between the lensing-inferred mass center and the brightest cluster galaxy is well fitted by a Gaussian distribution with width of $\sim 100 h^{-1}$ kpc, a scale comparable to the positional uncertainties in the lensing analysis. For these clusters, the lensing data is consistent with the DLRGs lying in the center of mass of their host halos. However, in a few clusters, the DLRGs are clearly offset from the center of the potential with characteristic displacements of $\sim 400 h^{-1}$ kpc. Johnston et al. (2007) reached a similar conclusion: most DLRGs are in the centers of their halo; however, a handful are significant displaced. However, the results are not yet conclusive due to the limited statistics. In this paper, we employ the following two empirical models for a radial profile of DLRGs based on these observational implications:

$$p_{\text{off}}(r; M) = \begin{cases} \frac{1}{(2\pi)^{3/2} r_{\text{off}}^3(M)} \exp\left(-\frac{r^2}{2r_{\text{off}}^2(M)}\right), & \text{(Gaussian offset model),} \\ \frac{c_{\text{off}}^3}{4\pi r_{\text{vir}}^3} f \frac{1}{(c_{\text{off}} r / r_{\text{vir}})(1 + c_{\text{off}} r / r_{\text{vir}})^2}, & \text{(NFW offset model),} \end{cases} \quad (12)$$

where $f \equiv 1/[\ln(1 + c_{\text{off}}) - c_{\text{off}}/(1 + c_{\text{off}})]$ and the prefactor of each model is determined so as to satisfy the normalization condition $\int_0^{r_{\text{vir}}} 4\pi r^2 dr p_{\text{off}}(r) = 1$. These profiles are specified by one parameter (r_{off} or c_{off}), but differ in the shape. Note that r_{vir} is specified as a function of halo mass and redshift, and c_{off} differs from the concentration parameter of dark matter profile.

As a working example, we will employ $r_{\text{off}}(M) = 0.3r_s(M) = 0.3r_{\text{vir}}(M)/c_{\text{vir}}(M)$ for Gaussian DLRG radial distribution and $c_{\text{off}} = 20$ for NFW DLRG radial distribution as our fiducial models. Here r_s is the scale radius of dark matter NFW profile, and c_{vir} is the concentration parameter. For the following results we will use the simulation results in Duffy et al. (2008) to specify c_{vir} as a function of halo mass and redshift. Our fiducial model of $r_{\text{off}} = 0.3r_s$ gives $r_{\text{off}} \simeq 100$ kpc for halos of $10^{14} M_{\odot}$, consistent with the results in Oguri et al. (2010). Note that the typical offset of the DLRG from the center of the halo potential varies with halo mass.

Fig. 2 shows the Gaussian and NFW models for the radial profile of DLRGs inside a halo of mass $M = 10^{14} h^{-1} M_{\odot}$ and at $z = 0.45$. Note that for our fiducial model, $r_s \simeq 250 h^{-1}$ kpc. These profiles are much more centrally concentrated than a typical dark matter halo of this mass scale, represented by an NFW profile with $c = 4.3$.

The Fourier transforms of these radial profiles are analytic functions:

$$\tilde{p}_{\text{off}}(k; M) = \begin{cases} \exp[-r_{\text{off}}^2(M)k^2/2], & \text{(Gaussian model),} \\ f \left[\sin \eta \{ \text{Si}(\eta(1 + c_{\text{off}})) - \text{Si}(\eta) \} + \cos \eta \{ \text{Ci}(\eta(1 + \eta)) - \text{Ci}(\eta) \} - \frac{\sin(\eta c_{\text{off}})}{\eta(1 + c_{\text{off}})} \right], & \text{(NFW model),} \end{cases} \quad (13)$$

where $\eta = kr_{\text{vir}}/c_{\text{off}}$, and $\text{Si}(x)$ and $\text{Ci}(x)$ are the sine and cosine integral functions. The Fourier transform $\tilde{p}_{\text{off}}(k; M) \simeq 1$ on relevant scales.

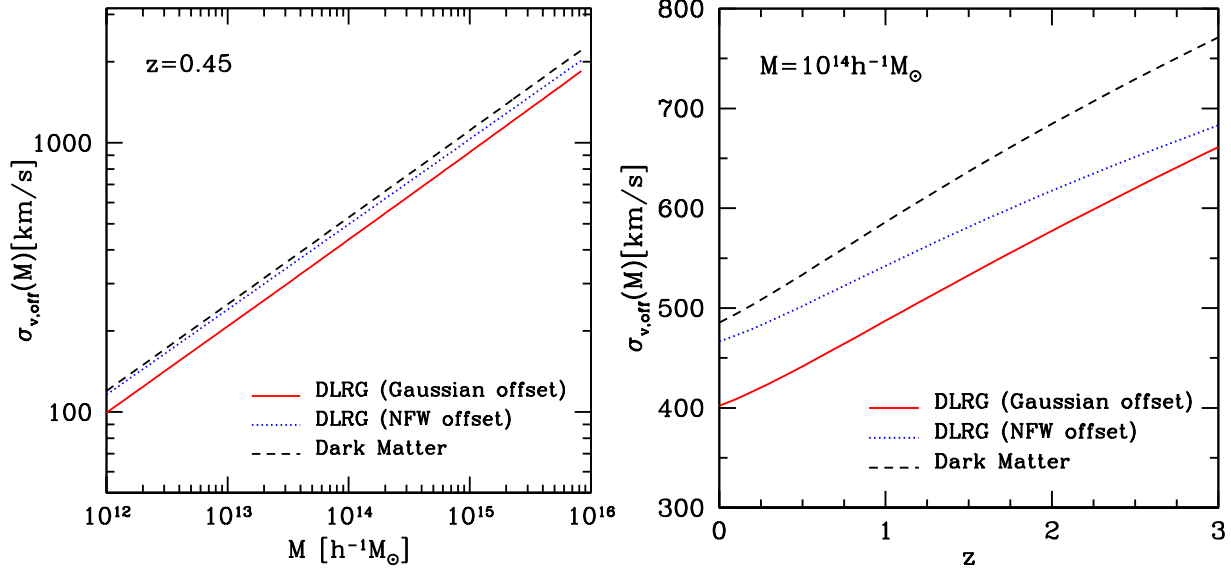


Figure 3. *Left panel:* Velocity dispersion of DLRGs averaged over DLRG radial profile, as a function of host halo mass at $z = 0.45$, assuming the Gaussian (solid curve) and NFW (dotted) radial profile profiles as in Fig. 2. For comparison the dashed curve shows the velocity dispersion of dark matter. *Right panel:* Redshift dependence of the velocity dispersions of DLRGs and DM for a halo with mass $M = 10^{14} h^{-1} M_{\odot}$.

2.3.3 Velocity dispersion of DLRGs

In this paper, we simply assume that galaxies at a given radius r have the following 1D velocity dispersion that is determined by the mass enclosed within the sphere:

$$\sigma_v^2(r; M) = \frac{GM(< r)}{2r}. \quad (14)$$

At virial radius r_{vir} , the velocity dispersion is determined by virial mass:

$$\sigma_v(r = r_{\text{vir}}; M) = 472 \text{ km/s} \left(\frac{M}{10^{14} h^{-1} M_{\odot}} \right)^{1/3} \left(\frac{\Delta(z)}{18\pi^2} \right)^{1/6} (1+z)^{1/2}, \quad (15)$$

where we use the definition of virial mass given in terms of the overdensity $\Delta(z)$ at redshift z (we use the fitting formulae given in Nakamura & Suto 1997). Since an NFW profile has an asymptotic behavior of $M(< r) \propto r^2$ as $r \rightarrow 0$, the velocity dispersion has the limit $\sigma_v(r; M) \rightarrow 0$ as $r \rightarrow 0$.

The velocity dispersion of LRGs is poorly known (see Skibba et al. 2011, for the first attempt). In Appendix A, we give an alternative model of computing the velocity dispersion by assuming an isothermal distribution for the phase space density of DLRGs within a halo, where we properly take into account the different radial profiles of DLRGs and dark matter.

The averaged velocity dispersion of DLRGs within halos of a given mass scale M can be obtained by averaging the velocity dispersion (Eq. [14]) with the radial profile of DLRGs:

$$\sigma_{v,\text{off}}^2(M) \equiv \int_0^{r_{\text{vir}}} 4\pi r^2 dr p_{\text{off}}(r; M) \sigma_v^2(r; M). \quad (16)$$

This velocity dispersion has an asymptotic limit when all the DLRGs are at the center of each halo: $\sigma_{v,\text{off}} \rightarrow 0$ when $p_{\text{off}}(r) \propto \delta_D(r)$. Fig. 3 plots the velocity dispersion of DLRGs, $\sigma_{v,\text{off}}(M)$, as a function of halo mass M for a fixed redshift (left panel), and as a function of redshift z for a fixed halo mass (right), respectively. The velocity dispersion of DLRGs is larger in more massive halos and at higher redshifts. Within the same halo, the velocity dispersion of DLRGs is smaller than that of dark matter by 10-20% in the amplitudes, because DLRGs are more centrally concentrated. Eq. (15) implies that the velocity dispersion of both the DLRGs and the dark matter scales as $\sigma_{v,\text{off}}(M) \propto M^{1/3}$.

2.4 Redshift-space power spectrum of DLRG and the covariance matrix

We use our model for the radial distribution of the DLRGs and their velocity distribution to estimate the effect of the offset on the power spectrum. We assume the velocity distribution of DLRGs within halos is Gaussian, where the width of the distribution is given by the velocity dispersion (Eq. [14]):

$$R(\Delta r_{\parallel}; r, M) d(\Delta r_{\parallel}) = \frac{1}{\sqrt{2\pi}\sigma_{v,\text{off}}(r, M)} \exp\left[-\frac{v_{\parallel}^2}{2\sigma_{v,\text{off}}^2(r, M)}\right] dv_{\parallel}, \quad (17)$$

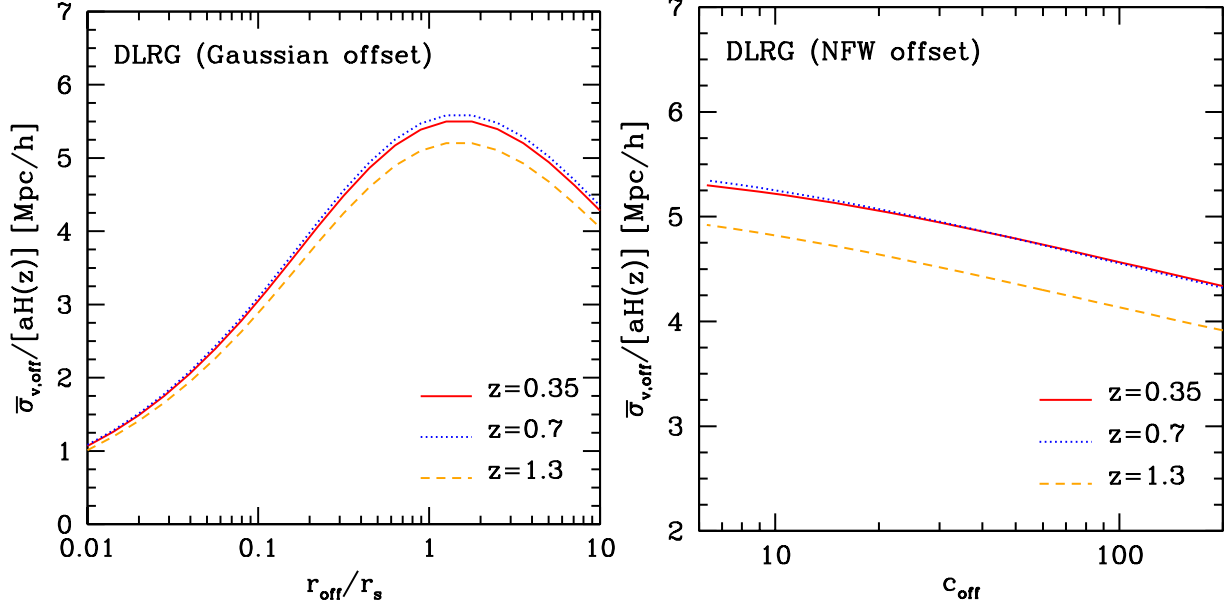


Figure 4. The FoG suppression scale (see Eq. [21]), $\bar{\sigma}_{v,off}/aH(z)$, as a function of the model parameters of DLRG radial profiles, for the Gaussian radial profile model (*left panel*) and the NFW model (*right panel*). The FoG scale is computed by averaging the velocity dispersion of DLRGs over the halo mass function weighted by the DLRG halo occupation distribution (Eq. [11]). The different curves are for different redshifts.

where $\Delta r_{\parallel} = v_{\parallel}/aH(z)$ and the prefactor is determined so as to satisfy $\int_{-\infty}^{\infty} d\Delta r'_{\parallel} R(\Delta r_{\parallel}; M) = 1$.

The Fourier transform of the redshift-space radial profile (see Eq. [6]) can be expressed as

$$\tilde{p}_{s,off}(k_{\perp}, k_{\parallel}; M) \simeq \int_0^{r_{vir}} 4\pi r^2 dr p_{off}(r; M) \exp\left[-\frac{\sigma_{v,off}^2(r, M) k^2 \mu^2}{2a^2 H^2(z)}\right], \quad (18)$$

where $k = \sqrt{k_{\perp}^2 + k_{\parallel}^2}$ and the exponential function above is the Fourier transform of Eq. (17). We again note that, exactly speaking, $\tilde{p}_{s,off}$ also depends on the Fourier transform of the real-space radial profile \tilde{p}_{off} as implied by Eq (6), but we use $\tilde{p}_{off} \simeq 1$ at large length scales of interest, much larger than the characteristic offset of the DLRG from the halo center. Also note that, for the limit $p_{off} \rightarrow \delta_D(r)$, $\tilde{p}_{s,off} \rightarrow 1$ as $\sigma_{v,off} \rightarrow 0$ at $r \rightarrow 0$.

Hence the redshift-space power spectrum of DLRGs (see Eq. [8]) can be computed for a given cosmological model by inserting Eq. (18) into

$$P_{s,DLRG}(k, \mu) = \left[\frac{1}{\bar{n}_{DLRG}} \int dM \frac{dn}{dM} b(M) N_{HOD}(M) \tilde{p}_{s,off}(k, \mu; M) \right]^2 P_{s,m}^{NL}(k, \mu). \quad (19)$$

At very large length scales (or very small k 's) the redshift-space power spectrum can be approximated as

$$P_{s,DLRG}(k, \mu) \approx \bar{b}^2 \left[1 - \frac{\bar{\sigma}_{v,off}^2 k^2 \mu^2}{a^2 H^2(z)} \right] P_{s,m}^{NL}(k, \mu), \quad (20)$$

where $\bar{\sigma}_{v,off}^2$ is the velocity dispersion averaged over the halo mass function weighted with the DLRG HOD:

$$\bar{\sigma}_{v,off}^2 \equiv \frac{1}{\bar{n}_{DLRG}} \int dM \frac{dn}{dM} b(M) N_{HOD}(M) \sigma_{v,off}^2(M). \quad (21)$$

As we will show below, the approximation (20) is not accurate at $k \gtrsim 0.15 h/\text{Mpc}$.

Thus the key quantity characterizing the FoG effect on DLRG power spectrum is the halo-mass averaged velocity dispersion, $\bar{\sigma}_{v,off}^2$. Table 1 gives the values for different redshifts assuming our fiducial model parameters. The DLRG velocity dispersion is also compared with that of dark matter within the same halos hosting DLRGs. It can be found that the typical FoG suppression scale, estimated as $\bar{\sigma}_{v,off}/(aH)$, is of scales of $5 h^{-1} \text{Mpc}$. Therefore, even at large length scales $k \simeq 0.1 h \text{Mpc}^{-1}$, which is employed in the literature in order to extract cosmological information, the FoG effect suppresses the power spectrum amplitudes by a factor of $0.75 (1 - [0.1 \times 5]^2 \simeq 0.75)$ according to Eq. (20), a systematic correction that is much larger than the reported statistical errors in many surveys (see Appendix C in Reid et al. 2010, for discussion).

Fig. 4 plots how the typical FoG suppression scale changes with changing parameters of the Gaussian and NFW DLRG radial profiles. For the Gaussian radial profile, the FoG displacement scale has a maximum scale of $\bar{\sigma}_{v,off}/(aH) \sim 5 h^{-1} \text{Mpc}$ around $r_{off} \sim r_s$, as the velocity dispersion peaks at the scale radius r_s for an NFW profile. On the other hand, for the NFW radial profile, the displacement scale

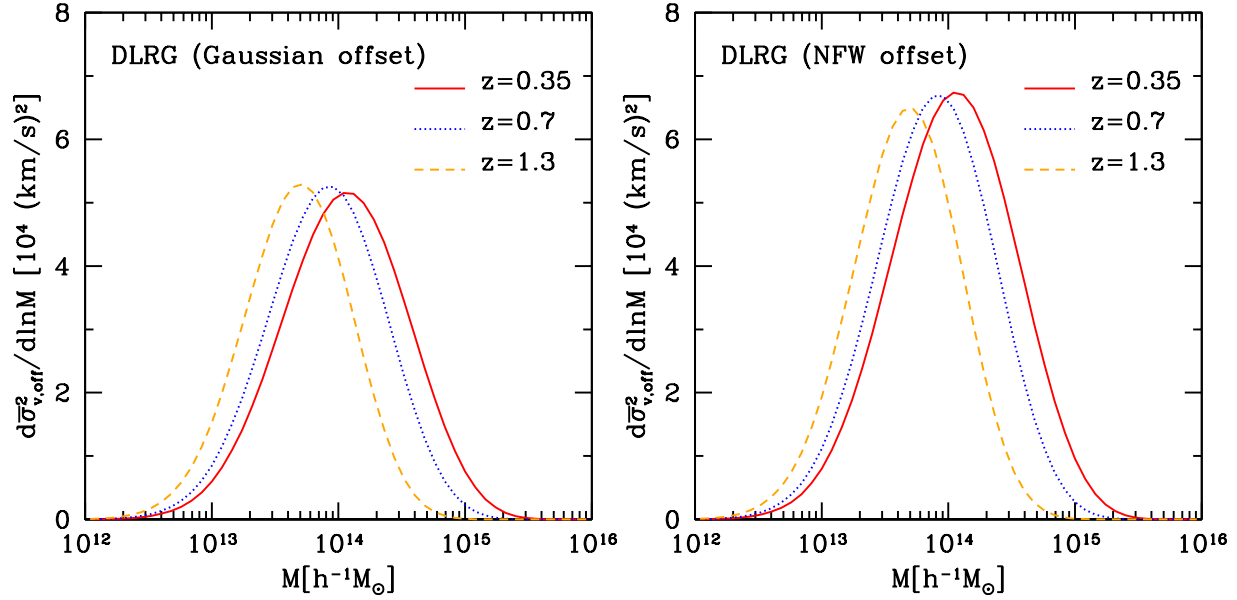


Figure 5. This figure shows how different mass halos contribute to the power spectrum suppression shown in Fig. 4. While the typical DLRG sits in a halo with mass $\sim 10^{13} M_{\odot}$, the FoG in the more massive halos plays the most important role in suppressing the galaxy power spectrum. The left and right panels are the results for the Gaussian and NFW radial profile profiles, respectively, where we assume the fiducial model parameters $r_{\text{off}} = 0.3r_s$ and $c_{\text{off}} = 20$, respectively, as in Fig. 2.

has a weak dependence on c_{off} , and leads to $\sim 5 h^{-1} \text{Mpc}$ over all the range of c_{off} . The redshift dependence of the FoG scale is weak and changes by only $\sim 10\%$.

Fig. 5 shows that the more massive halos are responsible for most of the FoG suppression. While the typical DLRG sits in halos of mass $5 \times 10^{13} h^{-1} M_{\odot}$, the FoG arises primarily from more massive halos as these halos have larger velocity dispersions. Here, we again assume the fiducial model parameters of the FoG effects as in Fig. 2. The plot shows that halos with masses $M \sim 10^{14} h^{-1} M_{\odot}$ have a dominant contribution to the FoG effect at redshifts $z = 0.35$ and 0.7 for both the Gaussian and NFW radial profiles, while less massive halos become more important at higher redshifts.

The covariance matrix describes statistical uncertainties in measuring the redshift-space power spectrum from a given survey, and the correlations between the power spectra of different wavenumbers. Takahashi et al. (2009) show that the assumption of Gaussian errors is valid on scales of interest. In this limit of Gaussian errors, the covariance matrix has a simple form:

$$\text{COV}[P_{s,\text{DLRG}}(k_i, \mu_a) P_{s,\text{DLRG}}(k_j, \mu_b)] = \frac{2\delta_{ij}^K \delta_{ab}^K}{N^{\text{mode}}(k_i, \mu_b)} \left[P_{s,\text{DLRG}}(k_i, \mu_b) + \frac{1}{\bar{n}_{\text{DLRG}}} \right]^2, \quad (22)$$

where k_i and μ_a are the i -th and a -th bins of wavenumber and cosine angle, respectively, and δ_{ij}^K and δ_{ab}^K are the Kronecker delta function: $\delta_{ij}^K = 1$ if $i = j$ within the bin width, otherwise $\delta_{ij}^K = 0$ and so on. The Kronecker delta functions impose that the power spectrum of different wavenumber bins are independent. The quantity $N^{\text{mode}}(k_i, \mu_a)$ is the number of independent Fourier modes around the bin centered at k_i and μ_a with widths Δk and $\Delta \mu$, which can be resolved for a given survey volume V_s : $N^{\text{mode}}(k_i, \mu_a) = 2\pi k_i^2 \Delta k \Delta \mu V_s / (2\pi)^3$. Here we assume the fundamental Fourier mode is determined by the survey volume as $k_f = 2\pi/L$, a reasonable approximation for a simple survey geometry.

3 ANGULAR POWER SPECTRUM OF DLRG-GALAXY WEAK LENSING

Observations of DLRG-galaxy lensing measure the radial distribution of DLRGs in the halo. In this subsection, we briefly review Oguri & Takada (2011) discussion of how the radial distribution of the DLRGs in their halo affects the galaxy-galaxy lensing observables.

The halos hosting DLRGs distort background galaxy images. By cross-correlating positions of DLRGs on the sky with tangential ellipticity component of background galaxy images with respect to the line connecting DLRG and background galaxy, we can measure the radially averaged mass distribution around a DLRG (Mandelbaum et al. 2006). While this stacking analysis is usually done in real space, we will describe the results in Fourier space as the effect of the DLRG offsets are convolution in real space and multiplication in Fourier space (Oguri & Takada 2011).

Since we are interested in small angular scales, we can use the flat-sky approximation (Limber 1954) and use the halo model in Oguri & Takada (2011) to compute the angular power spectrum of DLRG-galaxy lensing (also see Takada & Bridle 2007):

$$C_{\gamma g}(l) = C_{\gamma g}^{1h}(l) + C_{\gamma g}^{2h}(l), \quad (23)$$

where $C_{\gamma g}^{1h}$ and $C_{\gamma g}^{2h}$ are the 1- and 2-halo term spectra defined as follows. For the full-sky expression of the lensing power spectrum, see de Putter & Takada (2010). The 1-halo term contribution to galaxy-galaxy lensing arises from the mass distribution within one halo that hosts DLRGs and gives dominant contribution to the signal on small angular separations:

$$C_{\gamma g}^{1h}(l) \equiv \frac{1}{\bar{n}_{\text{DLRG}}^{2\text{D}}} \int d\chi \frac{d^2V}{d\chi d\Omega} S_{\text{DLRG}}(z) W^{\text{GL}}(\chi) \chi^{-2} \int dM \frac{dn}{dM} N_{\text{HOD}}(M) \frac{1}{\bar{\rho}_{m0}} \left[M \tilde{u}_{\text{NFW}}(k; M, z) \tilde{p}_{\text{off}}(k; M) \Big|_{k=l/\chi} + m_{\text{sh,DLRG}} \right], \quad (24)$$

where $\bar{\rho}_{m0}$ is the mean mass density today, χ is the comoving angular diameter distance (which is given as a function of redshift via the distance-redshift relation), $W^{\text{GL}}(\chi)$ is the lensing efficiency function for a given source galaxy population (see Eq. 19 in Oguri & Takada 2011), and $d^2V/d\chi d\Omega$ is the volume element in the unit comoving interval and the unit solid angle; $d^2V/d\chi d\Omega = \chi^2$ for a flat universe. The function $S_{\text{DLRG}}(z)$ is the redshift selection function of DLRGs. For simplicity, we assume a complete selection function: $S_{\text{DLRG}}(z) = 1$ within the redshift range of the survey, and otherwise $S_{\text{DLRG}} = 0$. The quantity $\bar{n}_{\text{DLRG}}^{2\text{D}}$ is the mean angular number density of DLRG in the redshift slice: $\bar{n}_{\text{DLRG}}^{2\text{D}} \equiv \int d\chi (d^2V/d\chi d\Omega) \int dM (dn/dM) N_{\text{HOD}}(M) S_{\text{DLRG}}(z)$. The term denoted by $m_{\text{sh,DLRG}}$ gives the contribution arising from a subhalo hosting DLRG, and we will throughout this paper assume the subhalo mass $m_{\text{sh,DLRG}} = 0.32 \times 10^{12} h^{-1} M_{\odot}$ as our fiducial value, implied from the results in Johnston et al. (2007).

There are two contributions to the 1-halo term in Eq. (24): the first term in the bracket describes the contribution of the halo of mass M and the second term describes the contribution of a subhalo hosting the DLRG. For the first term, we assume an NFW profile characterizing the dark matter distribution within a halo, and \tilde{u}_{NFW} is the Fourier-transform (see Eq. 29 in Oguri & Takada 2011). Including off-centered DLRGs in the galaxy-galaxy lensing analysis dilutes the measured lensing signal amplitudes at the small scales (Johnston et al. 2007; Oguri & Takada 2011). This off-centering effect on the lensing power spectrum can be included by simply replacing the dark matter profile with $\tilde{u} \tilde{p}_{\text{off}}$, where \tilde{p}_{off} is the Fourier-transformed coefficients of the DLRG radial profile (see Eq. [13]). For the subhalo contribution we simply assume the delta function for the mass profile, a good approximation at the relevant angular scales. In this limit, the power spectrum behaves like a white shot noise.

Similarly, the 2-halo term contribution, which dominates at large scales, is given as

$$C_{\gamma g}^{2h}(l) \equiv \frac{1}{\bar{n}_{\text{DLRG}}^{2\text{D}}} \int d\chi \frac{d^2V}{d\chi d\Omega} S_{\text{DLRG}}(z) W^{\text{GL}}(\chi) \chi^{-2} \left[\int dM \frac{dn}{dM} b(M) N_{\text{HOD}}(M) \right] P_m^L \left(k = \frac{l}{\chi}; z \right), \quad (25)$$

where $P_m^L(k)$ is the linear mass power spectrum. This 2-halo term scales with halo bias: if DLRGs are residing on more massive halos or equivalently more biased halos, the 2-halo term has greater amplitudes.

To perform parameter forecasts for planned lensing surveys, we also need to model the lensing power spectrum covariance. Following Takada & Jain (2009), we assume Gaussian errors so that the covariance matrix of the lensing power spectrum is given by a product of sampling variance and shot noise terms (see Oguri & Takada 2011, for the definition of the covariance matrix).

Fig. 6 shows the angular power spectrum of DLRG-galaxy weak lensing expected when cross-correlating DLRGs in redshift slice $0.3 < z < 0.4$ with background galaxy images that have a typical redshift of $z \sim 1$ as expected for a Subaru-type imaging survey. The top dotted curve shows the power spectrum when all DLRGs are at each halo's center, while the bold solid curves show the spectrum with the off-centering effect assuming our fiducial models of the Gaussian (*left panel*) and NFW (*right panel*) radial profiles as in Fig. 2. The figure shows that the off-centering effect significantly dilutes the lensing power spectrum amplitudes at angular separations smaller than the projected offset scale. The dashed curve shows the contribution from DLRG subhalo assuming $m_{\text{sh,DLRG}} = 0.32 \times 10^{12} h^{-1} M_{\odot}$. The DLRG subhalo contribution becomes significant at $l \gtrsim 2 \times 10^4$, where an angular scale of $l \sim 10^4$ corresponds to the projected scale ~ 300 kpc for the DLRG redshift of $z = 0.35$ for a Λ CDM model.

The boxes around the curve show statistical uncertainties in measuring band powers at each multipole bins, expected when measuring the DLRG-galaxy lensing for an overlapping area of 2000 square degrees between spectroscopic and imaging surveys. Here we assume the depth expected for Subaru HSC survey that probes galaxies at typical redshifts of $z_s \sim 1$ (see Section 4.1 for details). The plot clearly implies that combining such imaging and spectroscopic surveys allows us to infer the off-centering effect at a high significance. We will below give a more quantitative estimate.

4 RESULTS

In this section, we estimate the ability of ongoing and planned surveys for using the DLRG-galaxy weak lensing measurements to correct the FoG effect on redshift-space power spectrum of DLRGs.

4.1 Survey parameters

To model the DLRG power spectrum available from ongoing and upcoming spectroscopic surveys we assume survey parameters that resemble BOSS, Subaru PFS, and Euclid surveys. The expected statistical uncertainties in measuring the DLRG power spectrum in each redshift slice depend on the area coverage (or equivalently the comoving volume) and the number density and bias parameter of DLRGs. For the sky

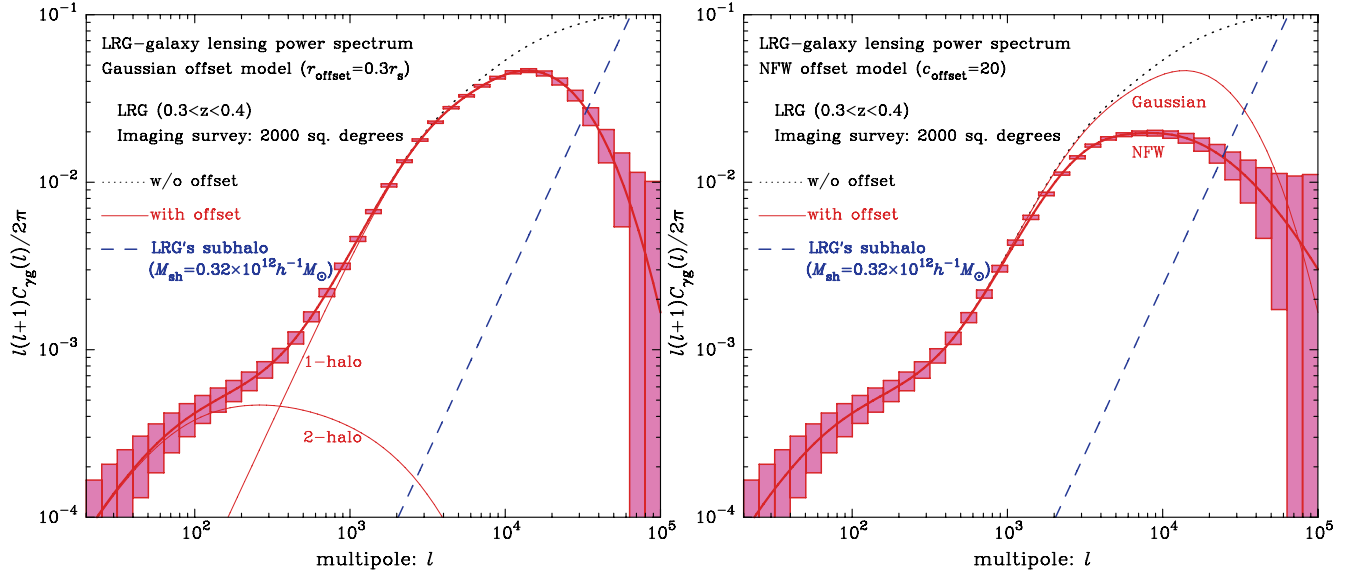


Figure 6. Angular power spectra of DLRG-galaxy lensing assuming that spectroscopic and imaging surveys are available for an overlapping area of 2000 square degrees and the DLRGs are in the redshift range of $0.3 < z < 0.4$ (see Section 4.1 for details). The bold solid curves are the angular power spectra including the off-centering effect for the Gaussian (*left panel*) and NFW (*right panel*) DLRG radial profiles. The thin curves in the left panel are the 1- and 2-halo term contributions. For comparison, the dotted curves are the spectra without the off-centering effect. The dashed curves are the contribution from a subhalo hosting DLRG, assuming the subhalo mass $m_{\text{sh,DLRG}} = 0.32 \times 10^{12} h^{-1} M_{\odot}$. The boxes around the bold solid curve are the expected 1σ uncertainties in measuring band powers of the power spectrum at each l bins, where we assume survey parameters given in Table 1.

coverage we assume 10,000, 2,000, and 20,000 square degrees for the BOSS, PFS, and Euclid surveys, respectively. Table 1 summarizes the survey parameters. For the redshift slices we consider 3 redshift bins with width $\Delta z = 0.1$ over the range $0.3 < z < 0.6$ for the BOSS survey, 4 slices with $\Delta z = 0.2$ over $0.6 < z < 1.4$ for the PFS survey, and 10 slices with $\Delta z = 0.1$ over $0.5 < z < 1.5$ for the Euclid survey. Thus the BOSS and PFS surveys are complementary to each other in their redshift coverages, while Euclid survey covers a wide range of redshifts on its own. Having a wider redshift coverage allows us to trace the redshift evolution of mass clustering growth over a wider range of redshifts and therefore improves cosmological constraints (Takada et al. 2006). In Table 1 we also show the comoving volume of each redshift slice. We simply assume the same HOD model given in Eq. (11) over all the redshifts to estimate the number density of DLRGs and the mean bias. The number densities are somewhat smaller than those actually obtained from data (e.g., White et al. 2011) or the target number densities for the survey. This is because we use the HOD model for DLRGs: we assume that we can select one DLRG per each halo based on the method of Reid et al. (2010). Table 1 also shows the FoG displacement scale $\bar{\sigma}_{v,\text{off}}/(aH)$ in each redshift slice, which is estimated using Eq. (21).

The parameter forecast is also sensitive to the maximum wavenumber k_{max} , because complex non-linearities alter the power spectrum at high wavenumber. In our analysis, we use Taruya et al. (2009, 2010) to determine k_{max} :

$$\frac{k_{\text{max}}^2}{6\pi^2} \int_0^{k_{\text{max}}} dk P_m^L(k) = C. \quad (26)$$

We use either $C = 0.2$ or 0.7 , motivated by the fact that the model predictions based on the standard and improved perturbation theory are sufficiently accurate in a sense that the predictions well match N-body simulation results to a few % accuracies in the amplitudes up to the determined k_{max} . Table 1 gives the k_{max} values for $C = 0.2$ and 0.7 , respectively, in each redshift slice. The approach in our analysis is to assume that refined model prescriptions based on N-body simulations (Taruya et al. 2010) are used to estimate non-linearities in the real space power spectrum and focus on the FoG effects on the DLRG power spectrum. Our goal is to show how the lensing analysis can calibrate the FoG effects.

For our analysis, we assume a lensing survey with either the properties of the planned Subaru HSC survey or the proposed EUCLID imaging survey. For the Subaru HSC survey we assume the survey area $\Omega_s = 2,000$ square degrees, the mean number density of imaging galaxies $\bar{n}_g^{\text{imaging}} = 30 \text{ arcmin}^{-2}$, and the redshift distribution is given by the functional form $n_g(z) \propto z^2 \exp(-z/z_0)$ where the parameter z_0 is determined so that the mean redshift $\langle z \rangle = 1$. For the Euclid survey we simply assume the same survey parameters, except for the survey area of $\Omega_s = 20,000$ square degrees. When computing the DLRG-galaxy lensing we use background galaxies at redshifts $z > z_{\text{DLRG},i} + \Delta z/2 + 0.05$, where $z_{\text{DLRG},i} + \Delta z/2$ is the upper bound on redshifts of DLRGs in the i -th redshift slice of a given spectroscopic survey. That is, we include galaxies at redshifts higher than the redshifts of any DLRGs in a given redshift slice by $\delta z = 0.05$. We assume that such background galaxies can be selected based on their available photometric redshift estimates (Nishizawa et al. 2010). In

Parameters of Spectroscopic Surveys

Survey	z	V_s [(Gpc/h) ³]	$k_{\max, C=0.2}$ [h/Mpc]	$k_{\max, C=0.7}$ [h/Mpc]	\bar{n}_{DLRG} [(h/Mpc) ³]	\bar{b}	\bar{M}_h [10 ¹⁴ M_\odot /h]	$\bar{\sigma}_{v,\text{off}}/aH(z)$ [Mpc/h]		
								DM	DLRG (Gauss)	DLRG (NFW)
BOSS (10,000 deg ²)	0.3 – 0.4	0.76	0.10	0.17	1.25×10^{-4}	1.80	0.63	5.35	4.42	5.06
	0.4 – 0.5	1.14	0.10	0.18	1.15×10^{-4}	1.85	0.58	5.41	4.48	5.10
	0.5 – 0.6	1.53	0.11	0.19	1.05×10^{-4}	1.89	0.54	5.43	4.50	5.11
PFS (2,000deg ²)	0.6 – 0.8	0.84	0.11	0.20	0.91×10^{-4}	1.95	0.48	5.42	4.49	5.07
	0.8 – 1.0	1.13	0.12	0.22	0.72×10^{-4}	2.02	0.42	5.33	4.43	4.97
	1.0 – 1.2	1.37	0.13	0.23	0.57×10^{-4}	2.08	0.36	5.20	4.32	4.81
	1.2 – 1.4	1.56	0.14	0.25	0.44×10^{-4}	2.14	0.31	5.03	4.19	4.64
Euclid (20,000deg ²)	0.5 – 0.6	3.06	0.11	0.19	1.05×10^{-4}	1.89	0.54	5.43	4.50	5.11
	0.6 – 0.7	3.84	0.11	0.20	0.95×10^{-4}	1.93	0.50	5.56	4.60	5.09
	0.7 – 0.8	4.60	0.12	0.20	0.86×10^{-4}	1.96	0.46	5.53	4.59	5.05
	0.8 – 0.9	5.32	0.12	0.21	0.77×10^{-4}	2.00	0.43	5.49	4.56	5.00
	0.9 – 1.0	5.98	0.13	0.22	0.69×10^{-4}	2.04	0.40	5.43	4.51	4.93
	1.0 – 1.1	6.58	0.13	0.23	0.61×10^{-4}	2.07	0.37	5.36	4.45	4.85
	1.1 – 1.2	7.11	0.14	0.24	0.54×10^{-4}	2.10	0.34	5.28	4.39	4.77
	1.2 – 1.3	7.58	0.14	0.25	0.47×10^{-4}	2.13	0.32	5.20	4.33	4.68
	1.3 – 1.4	8.00	0.15	0.26	0.41×10^{-4}	2.16	0.30	5.11	4.26	4.59
1.4 – 1.5	8.35	0.15	0.26	0.36×10^{-4}	2.18	0.28	5.01	4.18	4.50	

Table 1. Survey parameters considered in this paper, which are chosen to resemble the ongoing BOSS survey, and the planned Subaru PFS survey and Euclid survey. The range of redshift z , the survey volume of each redshift slice V_s , the mean number density of DLRGs \bar{n}_{DLRG} , the effective linear bias \bar{b} , and the mean halo mass \bar{M}_h are given. The quantity $k_{\max, C=0.2}$ or $k_{\max, C=0.7}$ is the maximum wavenumber of each redshift slice up to which the power spectrum information is included when studying parameter forecasts. The maximum wavenumbers are chosen by setting $C = 0.2$ or 0.7 in Eq. (26), which is motivated by the fact that there are accurate model predictions of halo clustering available up to such scales. The last three columns denote the FoG suppression scale, $\bar{\sigma}_{v,\text{off}}/aH(z)$ [Mpc/h], for dark matter and for DLRGs having the Gaussian and NFW radial profiles.

addition we assume the rms intrinsic ellipticities $\sigma_\epsilon = 0.22$ per component, which determines the intrinsic ellipticity noise contamination to the error covariance matrix of the DLRG-galaxy lensing power spectrum (Oguri & Takada 2011).

4.2 Weak lensing information on the off-centered DLRGs

In this subsection, we estimate the ability of future lensing survey to determine the radial distribution of DLRGs in the halos.

As shown in Fig. 6, the offset of the DLRGs from the centers of their halos dilutes the lensing signals at small angular scales. Thus if we assume that the dark matter halos are well-described by NFW halos on the ~ 100 kpc scale, the lensing observations can be used to infer the DLRG radial distribution.

There are two approaches that can be considered. The first one is a method fully based on the halo model. That is, by fitting the measured lensing profile to the halo model prediction (see Eq. [24]), one can constrain parameters including the parameters of either Gaussian or NFW DLRG radial profile model:

$$p_\alpha \equiv \{r_{\text{off}}(\text{Gauss}) \text{ or } c_{\text{off}}(\text{NFW}), c_N, \beta, \sigma_{\log M}, m_{\text{sh,DLRG}}\}, \quad (27)$$

where r_{off} or c_{off} is the off-centering parameter (see Eq. [12]), $\sigma_{\log M}$ is the parameter of DLRG HOD (see Eq. [11]), and the mean mass scale of subhalo hosting each DLRG (see Eq. [24]). The parameters c_N and β are introduced to model the scaling relation of halo concentration with halo mass, $c_{\text{vir}}(M_{\text{vir}}) = c_N (M_{\text{vir}}/10^{12} h^{-1} M_\odot)^{-\beta}$, where $c_N = 7.85$ and $\beta = 0.081$ are adopted for the fiducial values. Note that the HOD models are given by the two parameters $\sigma_{\log M}$ and M_{min} , but one of the two is determined by the observed mean number density of DLRGs. In this parameter estimation we assume that the halo mass function, halo bias and NFW profile or more generally halo mass profile are well calibrated based on a suite of simulations. We also assume that, although the lensing strength depends on cosmology, the background cosmology is well constrained from other cosmological observables such as CMB and the galaxy redshift survey itself (e.g., via the BAO experiment). Hence we include only the 1-halo term power spectrum of DLRG-galaxy lensing to perform the parameter forecast based on the Fisher matrix formalism.

We can use external information as priors on the model parameters. For the concentration-mass scaling relation, simulation-based studies (Duffy et al. 2008) and/or cluster lensing studies (Okabe et al. 2010) can be used as the priors. For the HOD parameter, $\sigma_{\log M}$, the clustering analysis of DLRGs (White et al. 2011) can be used. We employ the priors $\sigma(\ln c_N) = \sigma(\ln \beta) = \sigma(\ln \sigma_{\log M}) = 0.2$ in our Fisher analysis.

Table 2 gives the marginalized errors on the parameter, r_{off} or c_{off} , for the Gaussian or NFW radial profile model, respectively, in each redshift slice. Here we assume the DLRG-galaxy lensing measurements for an area of 2,000 or 20,000 square degrees for the Subaru HSC or Euclid survey, respectively, as discussed in § 4.1. Note that we include the lensing information up to $l_{\text{max}} = 5 \times 10^4$ in our Fisher analysis,

Off-centering Parameter Determination from DLRG-Galaxy Lensing					
Survey	Redshift range	Gaussian offset		NFW offset	
		$\sigma(\ln r_{\text{off}})$	$\sigma(\ln \bar{\sigma}_{v,\text{off}})$	$\sigma(\ln c_{\text{off}})$	$\sigma(\ln \bar{\sigma}_{v,\text{off}})$
BOSS (10,000 deg ²)	0.3 – 0.4	0.07	0.019	0.31	0.016
	0.4 – 0.5	0.08	0.022	0.33	0.018
	0.5 – 0.6	0.10	0.027	0.34	0.019
PFS (2,000 deg ²)	0.6 – 0.8	0.12	0.032	0.34	0.020
	0.8 – 1.0	0.24	0.066	0.36	0.022
	1.0 – 1.2	0.49	0.15	0.39	0.024
	1.2 – 1.4	0.85	0.33	0.46	0.030
Euclid (20,000 deg ²)	0.5 – 0.6	0.058	0.016	0.22	0.012
	0.6 – 0.7	0.087	0.024	0.24	0.014
	0.7 – 0.8	0.13	0.036	0.27	0.015
	0.8 – 0.9	0.20	0.055	0.29	0.017
	0.9 – 1.0	0.31	0.086	0.31	0.019
	1.0 – 1.1	0.47	0.14	0.33	0.020
	1.1 – 1.2	0.71	0.24	0.35	0.022
	1.2 – 1.3	1.03	0.51	0.37	0.023
	1.3 – 1.4	1.44	0.53	0.39	0.025
1.4 – 1.5	1.87	0.54	0.41	0.027	

Table 2. Marginalized uncertainties in the DLRG off-centering parameters in each redshift slice, which are expected to obtain from the DLRG-galaxy lensing measurements (see around Eq. [27] for details of our Fisher analysis). For the BOSS and PFS surveys, we assume that the Subaru HSC-type imaging survey is overlapped with the spectroscopic surveys for an area of 2000 square degrees. For the Euclid survey we assume the overlapping area of 20000 square degrees for the joint imaging and spectroscopic surveys. As in Fig. 2 we consider the Gaussian or NFW DLRG radial profiles as a working example, and the error bars show the relative errors: e.g., $\sigma(\ln r_{\text{off}}) \equiv \sigma(r_{\text{off}})/r_{\text{off}}$, where the denominator is the fiducial value. The relative error on the FoG suppression scale, denoted by $\sigma(\ln \sigma_{v,\text{off}})$, is estimated by propagating the error of r_{off} or c_{off} using Eq. (21).

but we find that the results in Table 2 are not so sensitive to the choice of the maximum multipole as such small-scale signals are dominated by the lensing contribution of DLRG’s subhalo. Most of the information on the characteristic offsets comes from the power spectrum at $l \lesssim 10^4$. Table 2 also shows the expected error on the FoG suppression scale, which is obtained by propagating the error of the characteristic offset based on Eq. (21).

The method above is a model-dependent method. Since the Gaussian or NFW radial profile models may differ from the genuine radial profile, the estimated offset parameters may have systematic biases. Moreover the radial profile may change with halo masses. Hence an alternative approach is based on a method that the measured lensing profile is compared with an single NFW profile, including the off-centering effect. Previous measurements (Johnston et al. 2007; Okabe et al. 2010) mostly used this method. However, we find that this method does not work well if we use the full sample of DLRGs for the DLRG-galaxy lensing measurements. If the lensing profile in Fig. 6 is fitted to a single NFW profile, the extracted halo mass is found to be $\sim 0.5 \times 10^{14} h^{-1} M_{\odot}$, i.e. the mean halo mass of halos hosting DLRGs as listed in Table 1. This mass scale is smaller than the mass scale of halos, $10^{14} h^{-1} M_{\odot}$, that give a dominant contribution to the FoG effect as shown in Fig. 5. In turn the characteristic offset inferred from such a single NFW profile-fitting is not that accurate. Since the FoG effects are larger for the more massive halos, it would be more optimal to focus on studies of the DLRG-galaxy lensing for halos with a narrower mass range around $10^{14} h^{-1} M_{\odot}$, where such a halo catalog can be constructed based on optical richness available from multi-color imaging survey itself, X-ray and/or Sunyaev-Zel’dovich (SZ) data.

In fact we are now working on the SDSS DR7 LRG catalog in order to explore the feasibility of the method above with real data. In this on-going study, we have focused on the regions including multiple LRGs in the small spatial region, which are likely to reside in the same halo with masses more massive than other majority of halos hosting a single LRG inside. We have then studied the galaxy-galaxy lensing signal measured via cross-correlation of the LRG regions with background galaxy shapes, where the background galaxies are taken from the photometric SDSS galaxy catalog based on their photometric redshift estimates. We have so far found, preliminarily though, that the lensing signals at small scales do change with different centers; the brightest LRG position, the faintest LRG or the mean of their positions. Then we are now trying to constrain the off-centered profile of LRGs from the varied lensing signals including marginalizations over other parameters such as the mean halo mass, the halo profile parameters and the sub-halo mass scale. This is in working progress, and will be presented elsewhere (Hikage et al. in prep.).

In this paper, we will just assume that the first approach stated above, i.e. the halo model based fitting method, is feasible for the following analysis.

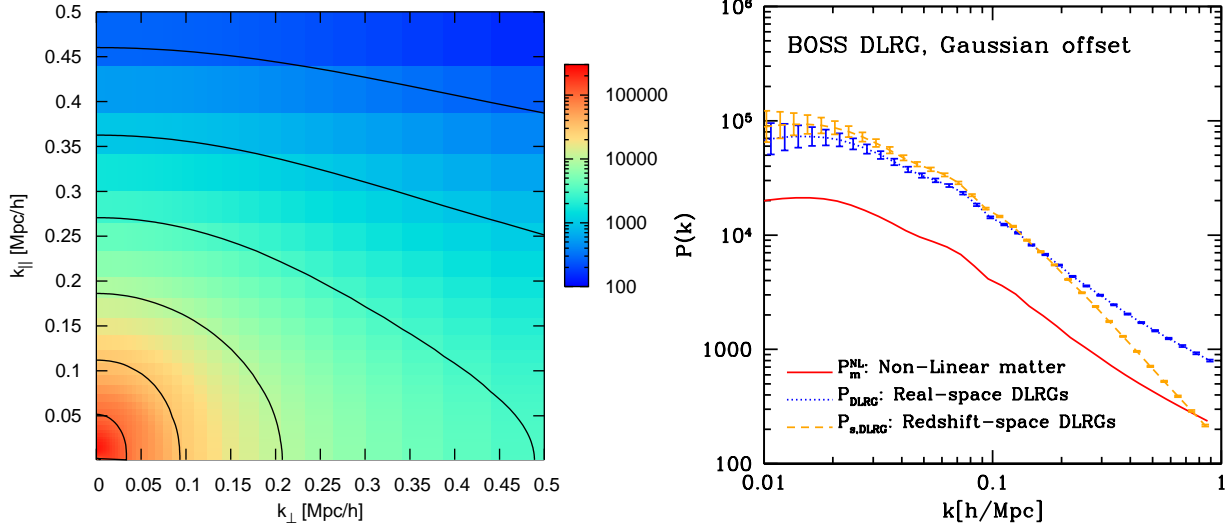


Figure 7. *Left panel:* Redshift-space power spectrum of DLRGs, $P_{s,\text{DLRG}}(k_{\parallel}, k_{\perp})$, in the two-dimensional wavenumber space $(k_{\parallel}, k_{\perp})$. We use Eq. (8) to compute the power spectrum assuming the Gaussian DLRG radial profile in Fig. 2, and assume the parameters expected for BOSS survey in Table 1. The spectrum shown is the spectra averaged over the redshift range $0.3 \leq z \leq 0.6$. The contours denote the power spectrum amplitudes of $10^5, 3.2 \times 10^4, 10^4, 3.2 \times 10^3, 10^3, 3.2 \times 10^2, 10^2$ $(h/\text{Mpc})^3$, respectively. *Right panel:* The monopole power spectrum of DLRGs obtained by averaging the redshift-space power spectrum over the angle $\mu (\equiv k_{\parallel}/k)$ for a fixed $k (\equiv \sqrt{k_{\perp}^2 + k_{\parallel}^2})$. For comparison, the non-linear matter power spectrum $P_m^{\text{NL}}(k)$ and the real-space power spectrum of DLRGs (Eq. [2]) are plotted. The error bars show the 1σ statistical errors in measuring the power spectrum at each k bin for BOSS survey.

4.3 The FoG effect on DLRG power spectrum

In this subsection, we explore how the off-centered DLRGs suppress the power spectrum through their FoG effects. The left panel of Fig. 7 shows the DLRG power spectrum $P_{s,\text{DLRG}}(k_{\perp}, k_{\parallel})$ (Eq. [8]) in the two-dimensional space of $(k_{\perp}, k_{\parallel})$ assuming the Gaussian DLRG radial profile model. The plotted power spectrum is the spectra averaged over a range of redshifts, $0.3 \leq z \leq 0.6$, covered by the BOSS survey. Apparent anisotropic features can be found: at large length scales ($k \lesssim 0.15 h/\text{Mpc}$), the Kaiser effect enhances the power along the line-of-sight direction, while the FoG effect suppresses the power more significantly with increasing wavenumbers and thus squashes the contours along k_{\parallel} . The right panel shows the monopole power spectrum which is obtained by averaging the redshift-space power spectrum over the angle $\mu (\equiv k_{\parallel}/k)$ for a fixed $k (\equiv \sqrt{k_{\perp}^2 + k_{\parallel}^2})$. For comparison we also show the real-space DLRG power spectrum $P_{\text{DLRG}}(k)$ (Eq. [2]) and the input non-linear matter power spectrum $P_m^{\text{NL}}(k)$, where the latter is computed using the fitting formula by Smith et al. (2003). It is clear that the redshift-space distortion effect causes a scale-dependent modification in the amplitude as well as shape of monopole power spectrum.

To be more quantitative, Fig. 8 shows the ratio between the monopole spectra of redshift- and real-space DLRG power spectra as a function of k . Since the linear Kaiser redshift distortion causes an overall offset in the monopole power spectrum amplitudes, the scale-dependent effect in the figure is solely due to the FoG effect. The data points show the DLRG power spectrum assuming the Gaussian radial profile model. The error bars are the expected 1σ statistical uncertainties in measuring band powers of the power spectrum at each k bin for the BOSS survey, which include the sampling variance and shot noise contamination. The plot implies that the FoG effect can be very significant even at very large length scales, $k \simeq 0.1 h\text{Mpc}^{-1}$, relevant for BAO scales, and the FoG suppression is more significant at larger k 's. The FoG effect suppresses the power spectrum amplitudes by 10 (30%) around $k = 0.1(0.2) h\text{Mpc}^{-1}$.

The following empirical models of the FoG effect are often assumed in the literature:

$$\begin{aligned} \text{Gaussian :} & \quad \exp[-(k\mu\bar{\sigma}_{v,\text{off}}/aH(z))^2], \\ \text{Lorentzian :} & \quad \frac{1}{1 + (k\mu\bar{\sigma}_{v,\text{off}}/aH(z))^2}, \end{aligned} \tag{28}$$

which are called the Gaussian and Lorentzian FoG models. These two models are given by a single parameter $\bar{\sigma}_{v,\text{off}}$ and have the same form given as $1 - (k\mu\bar{\sigma}_{v,\text{off}}/aH)^2$ at the small k limit. Note that we use the same notation $\bar{\sigma}_{v,\text{off}}$ as that of the radial profile model for notational simplicity, but keep in mind that $\bar{\sigma}_{v,\text{off}}$ in the equation above is a free model parameter.

The dashed and dotted curves in Fig. 7 show the results for these FoG models, which can be compared with the FoG effect due to off-centered DLRGs we have developed in this paper. Here the model parameter $\bar{\sigma}_{v,\text{off}}$ is taken from Eq. (21) assuming the input Gaussian radial profile model. At scales $k \lesssim 0.15 h\text{Mpc}^{-1}$, all the results well agree with each other because the FoG effect can be well approximated as $1 - (k\mu\bar{\sigma}_{v,\text{off}}/aH)^2$ at such small k 's. At the larger k 's the model differences become significant: the Gaussian approximation underestimates

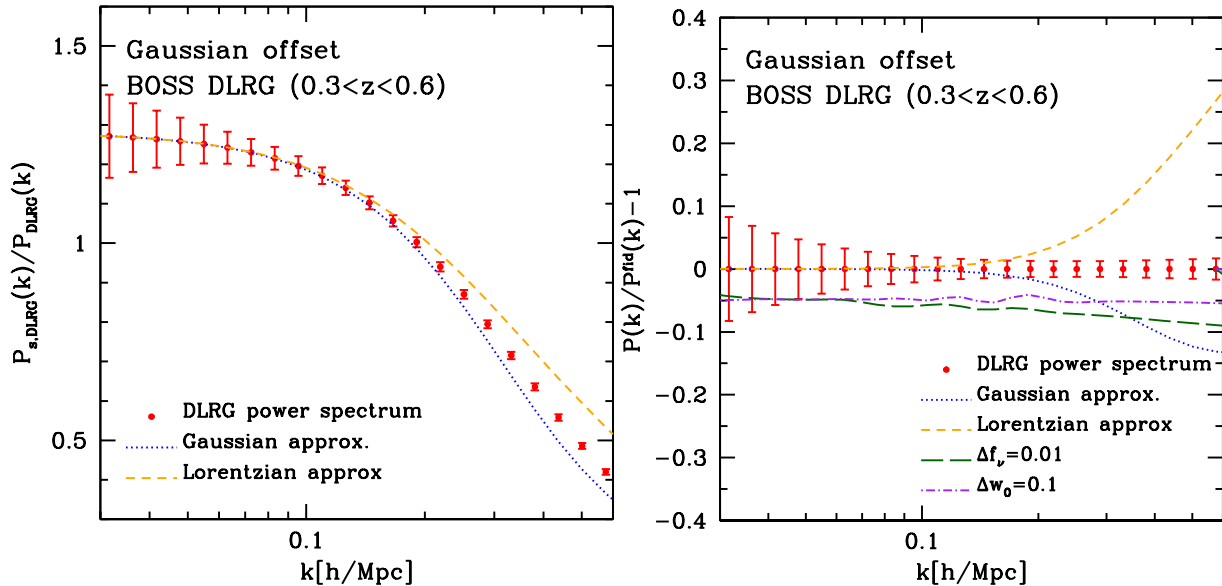


Figure 8. *Left panel:* The relative difference between the monopole redshift-space power spectra of DLRGs with and without redshift distortion effect (the linear Kaiser effect plus the FoG effect). The data at each k bins shows the halo model predictions we have developed in this paper, and the error bar at each k -bin shows the 1σ statistical uncertainties of the band power expected from the BOSS survey (see Table 1). For comparison, the dotted and dashed curves show the model predictions assuming a Gaussian or Lorentzian FoG form (see Eq. [28]), which is specified with a single parameter $\bar{\sigma}_{v,off}$ (Eq. [21]). The full halo model prediction and the approximations show differences greater than the statistical error, more significantly at higher k 's. *Right panel:* The difference ratio of the power spectra between the full FoG effect and the approximated FoG effects (Gaussian or Lorentzian FoG models): $P_{s,DLRG}^{app}/P_{s,DLRG}^{full} - 1$. Also shown is how the redshift-space power spectrum changes with changing the dark energy equation of state parameter w_0 and the neutrino mass f_ν ($\equiv \Omega_{\nu 0}/\Omega_{m0}$): here we consider variations to $w_0 = -0.9$ and $f_\nu = 0.01$ (corresponding to the total neutrino mass $m_{\nu,tot} = 0.104$ eV) from the fiducial values $w_0 = -1$ and $f_\nu = 0$, respectively.

the power, while the Lorentzian overestimates the power. The differences arise because the FoG effect in our model arises after the integration of halo mass function and the DLRG radial profile (see Eqs. [18] and [19]), and therefore the resulting FoG effect does not exactly follow a Gaussian form, even if we assume that the velocity probability distribution of DLRGs is Gaussian for each halos.

The right panel of Fig. 8 more explicitly shows the relative differences between the FoG effect and the FoG approximations (Eq. [28]). The plot shows that either Gaussian or Lorentzian FoG model cannot be accurate enough compared to the accuracies of upcoming galaxy surveys. The plot also shows how the monopole power spectrum changes with changing the dark energy equation of state parameter to $w_0 = -0.9$ from $w_0 = -1$ or the neutrino mass to $f_\nu = 0.01$ ($m_{\nu,tot} = 0.104$ eV) from $f_\nu = 0$. These parameters are both sensitive to the power spectrum amplitudes and therefore most affected by the FoG uncertainty as we will study below more extensively. The plot shows that the upcoming surveys have a much higher statistical precision than the effects due to these parameter changes, and also shows that a correction/calibration of the FoG effect is very important in order not to have a biased estimate on these parameters. Finally, for the FoG effect due to the NFW radial profile model, we have also found similar results to the results in Fig. 8.

The amount of the FoG suppression effect shown in Fig. 8 obviously depends on the fiducial parameters of our FoG model. One of the model uncertainties is the velocity distribution of DLRGs within a halo. If we use the model given in Appendix A, the FoG suppression effect is roughly half of the amplitude shown in Fig. 8. A full analysis of both simulations and observations will be essential to quantify the amplitude of this suppression. In the following analysis, for simplicity we will continue to assume the FoG effect computed using our fiducial Gaussian and NFW radial profile models.

4.4 The Impact of FoG Effect on Cosmological Parameter Estimations

How does an imperfect modeling of the FoG effect affect cosmological parameter estimation? In particular how can adding the DLRG-galaxy lensing information helps correct for the FoG effect on the redshift-space DLRG power spectrum? In this subsection, we address these questions.

We perform a Fisher analysis to estimate expected accuracies of parameters for upcoming galaxy surveys, and possible biases due to an imperfect modeling of the FoG effect. As the observable we use the redshift-space DLRG power spectrum. In the galaxy clustering analysis one needs to assume a reference cosmological model to infer the spatial position of each galaxy from the observed redshift and angular position. However, the assumed cosmology generally differs from the underlying true cosmology, which causes cosmological distortion effect on the observed power spectrum. Hence the observed redshift-space power spectrum can be given as (Alcock & Paczynski 1979; Seo & Eisenstein 2003):

$$P_{s,\text{DLRG}}^{\text{obs}}(k_{\parallel}^{\text{fid}}, k_{\perp}^{\text{fid}}) = \frac{D_A(z)_{\text{fid}}^2}{D_A(z)^2} \frac{H(z)}{H(z)_{\text{fid}}} P_{s,\text{DLRG}}(k_{\parallel}, k_{\perp}), \quad (29)$$

where $k_{\parallel}^{\text{fid}} \equiv (D_A/D_{A,\text{fid}})k_{\parallel}$, $k_{\perp}^{\text{fid}} \equiv (H_{\text{fid}}/H)k_{\perp}$, and $D_A(z)$ and $H(z)$ are the angular diameter distance and the Hubble expansion rate at redshift z . The quantities with subscript ‘‘fid’’ denote the quantities of the assumed reference cosmology. We use Eq. (19) to compute the redshift-space power spectrum.

Using the power spectrum covariance (Eq. [22]), the Fisher information matrix of the DLRG power spectrum measurement is computed as

$$F_{\alpha\beta}^{\text{DLRG}} \simeq \sum_{z_i} \frac{V_{z_i}}{8\pi^2} \int_{-1}^1 d\mu \int_{k_{\min}}^{k_{\max}} k^2 dk \frac{\partial \ln P_{s,\text{DLRG}}^{\text{obs}}(k, \mu; z_i)}{\partial p_{\alpha}} \frac{\partial \ln P_{s,\text{DLRG}}^{\text{obs}}(k, \mu; z_i)}{\partial p_{\beta}} \left[1 + \frac{1}{\bar{n}_{\text{DLRG}}(z_i) P_{s,\text{DLRG}}^{\text{obs}}(k, \mu; z_i)} \right]^{-2}. \quad (30)$$

where the summation is over redshift slices, V_{z_i} is the comoving volume of the i -th redshift slice, and p_{α} denotes a set of model parameters. The redshift ranges of each slice are given in Table 1. For each redshift slice, the minimum wavelength k_{\min} is set to be $2\pi/V_{z_i}^{1/3}$ and the maximum wavelength k_{\max} are chosen using the criterion given by Eq. (26) as listed in Table 1. As we discuss around Eq. (26), the impact of the FoG effect becomes more significant with including the power spectrum information up to the higher k_{\max} . We use a publicly available code CAMB (Lewis et al. 2000) to compute the input linear-mass power spectrum.

The galaxy power spectrum alone cannot determine all the cosmological parameters due to severe parameter degeneracies (Takada et al. 2006). Therefore, we combine CMB information with the galaxy power spectrum, which helps efficiently in breaking the parameter degeneracies. We use the CMB information expected from the Planck experiments: the temperature spectrum, E -mode polarization spectrum and the cross-spectrum over multipole range of $2 \leq l \leq 1500$. We compute the CMB Fisher matrix $F_{\alpha\beta}^{\text{Planck}}$ assuming the instrument noise and beam size of each frequency channel in the Planck website¹². The Fisher matrix for a joint experiment of the CMB and galaxy power spectra is simply estimated as $F_{\alpha\beta} = F_{\alpha\beta}^{\text{Planck}} + F_{\alpha\beta}^{\text{DLRG}}$. The marginalized error of the α -th parameter, $\sigma(p_{\alpha})$, is estimated as $(\mathbf{F}^{-1})_{\alpha\alpha}^{1/2}$, where \mathbf{F}^{-1} is the inverse matrix of the Fisher matrix \mathbf{F} .

The parameter estimation is sensitive to a set of model parameters as well as a choice of the fiducial model. We include a fairly broad range of model parameters:

$$p_{\alpha} \equiv \{\Omega_b h^2, \Omega_{\text{cdm}} h^2, \Omega_K, \Omega_{\text{DE}}, \tau, A, n_s, 1/\bar{n}(z_i), \bar{b}(z_i), r_{\text{off}}(z_i) \text{ or } c_{\text{off}}(z_i) \text{ or } \bar{\sigma}_{v,\text{off}}(z_i), f_{\nu} \text{ and/or } w_0 \text{ or } f_g(z = z_i)\}. \quad (31)$$

The first 7 parameters are cosmological parameters, and the fiducial values are given at the end of Section 1. Following Seo & Eisenstein (2003) (also see Saito et al. 2011), we include $1/\bar{n}(z_i)$ and $\bar{b}(z_i)$ as free parameters in order to model uncertainties due to the residual shot noise and galaxy bias in each redshift slice. The FoG effect fully computed based on the halo model is parametrized by the off-centering parameter in each redshift (Eq. [12]): $r_{\text{off}}(z_i)$ for the Gaussian radial profile model, or $c_{\text{off}}(z_i)$ for the NFW model. When we approximate the FoG effect with the Gaussian or Lorentzian form (Eq. [28]), we instead use $\bar{\sigma}_{v,\text{off}}(z_i)$ (Eq. [19]) as a parameter. The fiducial value of $\bar{\sigma}_{v,\text{off}}(z_i)$ is computed based on the halo model (eq.[21]).

In Eq. (31), we further include additional parameter(s): the dark energy equation-of-state parameter $w_0 (= 0)$ and/or the neutrino energy-density fraction $f_{\nu} \equiv \Omega_{\nu}/\Omega_m (= 0.01)$ ¹³, or the growth rate of each redshift slice $f_g(z_i) \equiv d \ln D / \ln a|_{z_i}$. The values in the parenthesis denote the fiducial values, and the fiducial values of f_g in each redshift slice are taken from those of our fiducial Λ CDM model. These parameters are all sensitive to the small-scale amplitudes of galaxy power spectrum, and therefore degenerate with the FoG suppression effect. We will pay special attention to an issue of how a knowledge of the FoG effect helps constrain these parameters and minimize a possible bias in the parameter caused by the FoG uncertainty. The dimension of our Fisher matrix is at most 19×19 , 23×23 , and 47×47 for BOSS, PFS and Euclid surveys, respectively.

In the parameter forecast we will consider the following four cases for the treatment of the FoG effect:

(i) The redshift-space power spectrum of DLRGs, measured from a hypothetical survey (BOSS, PFS or Euclid), is compared to the model power spectrum, which is given by the non-linear redshift-space matter power spectrum (Eq. [9]) multiplied with either Gaussian or Lorentzian FoG model (see Eq. [28]). In this fitting, the parameter $\bar{\sigma}_{v,\text{off}}$ of the FoG model is treated as a free parameter (we will hereafter call ‘‘w/o offset’’).

(ii) The similar approach to the case (i), but we employ the external information on $\bar{\sigma}_{v,\text{off}}$ from the DLRG-galaxy lensing measurements assuming combined imaging and spectroscopic surveys: the Subaru HSC survey combined with either BOSS or PFS survey or the combined Euclid imaging and spectroscopic surveys (we will call ‘‘with offset’’). To be more precise we use the statistical error on $\bar{\sigma}_{v,\text{off}}$ in Table 2 as the prior of the Fisher analysis.

(iii) This is fully based on the halo model approach: the FoG effect is computed based on the halo model (Eq. [19]) assuming either Gaussian or NFW radial profile model. We use the lensing-derived constraints on r_{off} (Gaussian) or c_{off} (NFW) listed in Table 2 as the prior of the Fisher analysis (we will call ‘‘FoG shape known’’).

¹² <http://www.sciops.esa.int/index.php?project=PLANCK>

¹³ The fiducial value $f_{\nu} = 0.01$ corresponds to the total neutrino mass $m_{\nu,\text{tot}} = 0.104\text{eV}$ for our fiducial Λ CDM model. This value is close to the lower limit if the neutrinos obey the inverted mass hierarchy.

(iv) This is the extreme case that we neglect the FoG effect in the parameter estimation by setting $\bar{\sigma}_{v,\text{off}}$ to be = 0 (we will call ‘‘FoG neglected’’).

Based on the Fisher matrix formalism, we estimate the bias due to an imperfect modeling of the FoG effect, $\delta p_\alpha (\equiv p_{\alpha,\text{est}} - p_{\alpha,\text{true}})$, the difference between the estimated and input values of the α -th parameter p_α . The amount of the bias is estimated as

$$\delta p_\alpha = \sum_{\beta} (\mathbf{F}^{-1})_{\alpha\beta} b_\beta, \quad (32)$$

where

$$b_\beta \equiv \sum_i \frac{V_{z_i}}{8\pi^2} \int_{-1}^1 d\mu \int_{k_{\text{min}}}^{k_{\text{max}}} k^2 dk \left[\frac{P_{s,\text{DLRG}}(k, \mu; z_i)}{P_{s,\text{DLRG}}^{\text{app}}(k, \mu; z_i)} - 1 \right] \frac{\partial \ln P_{s,\text{DLRG}}^{\text{app}}(k, \mu; z_i)}{\partial p_\beta} \left[1 + \frac{1}{\bar{n}_{\text{DLRG}} P_{s,\text{DLRG}}(k, \mu; z_i)} \right]^{-2}. \quad (33)$$

Here $P_{s,\text{DLRG}}$ denotes the true power spectrum where the FoG effect is computed based on the halo model. On the other hand, $P_{s,\text{DLRG}}^{\text{app}}$ is the approximated spectrum using Gaussian or Lorentzian FoG model. The total error including both statistical and systematic errors is estimated as

$$[\Delta p_\alpha]^2 = [\sigma_{\text{stat}}(p_\alpha)]^2 + (\delta p_\alpha)^2. \quad (34)$$

We estimate the impact of the FoG effect on the measurement of the growth rate in each redshift slice. Figs. 9 and 10 compare the marginalized, fractional errors of $f_g(z_i)$ for the cases (i) and (ii), the cases with and without the FoG effect correction using the DLRG-galaxy lensing information of the DLRG radial profile (see Table 2). The upper panels show the results for the Gaussian radial profile model, while the lower panels show the results for the NFW radial profile model. The left- and right-side panels are different in the maximum wavenumber k_{max} , which is determined by $C = 0.2$ (left panels) and $C = 0.7$ (right) in Eq. (26) roughly corresponding to $k_{\text{max}} \simeq 0.1$ and 0.2 hMpc^{-1} respectively (see Table 2). Note that the plotted errors include the statistical and systematic errors (Eq. [34]). It is found that the lensing information significantly improves the constraint on f_g over a wide range of redshifts z : the improvement is up to a factor of 2 for $C = 0.2$ (the lower k_{max}), but less significant at higher z . This result can be understood as follows. The DLRG-galaxy lensing measurements are more accurate for lower z DLRGs because of higher number densities of background galaxies, which reduces the shot noise contamination. (see Table 2). The error of f_g improves less at higher k where the systematic error due to the FoG model inaccuracy is dominated over the statistical error. The Gaussian FoG model gives a better improvement than the Lorentzian model because we assume the Gaussian velocity distribution of DLRGs within halos. Finally, comparing the upper- and lower-side panels shows that the NFW radial profile model gives a better performance of the lensing FoG correction, as implied by the accuracies of the DLRG velocity dispersion reconstruction in Table 2. As a result these spectroscopic surveys allow for constraints on the growth rate to 5% precision or even better at each redshift when the lensing information is combined.

Tables 3 and 4 study the impact of FoG effect on the parameter f_ν and w_0 , respectively. The tables show the marginalized error on each parameter and the amount of bias in the best-fit parameter if the FoG effect is corrected imperfectly or ignored. Note that in this analysis, either w_0 or f_ν is fixed to the fiducial value: for the table of w_0 , f_ν is fixed to $f_\nu = 0$ and vice versa. Although the dark energy equation-of-state parameter w_0 can be more robustly constrained by the BAO peak location (Eisenstein et al. 2005), adding the amplitude and shape information of power spectrum can significantly improve the error because dark energy is sensitive to the power spectrum amplitude via the growth rate (Saito et al. 2011). First of all, the table shows that the FoG effect is very significant even at such large length scales ($k_{\text{max}} \simeq 0.1 \text{ hMpc}^{-1}$ for $C = 0.2$). For example, the column ‘‘FoG neglected’’ indicates that the parameters are significantly biased if the FoG effect is ignored. The bias can be larger than the statistical error by more than a factor of 5. That is, if the FoG effect is ignored, a non-zero neutrino mass or $w_0 \neq -1$ may incorrectly be claimed.

The table also shows that the parameter accuracy of f_ν or w_0 can be improved by correcting for the FoG effect based on the lensing information of DLRGs radial profile. For $C = 0.2$ ($k_{\text{max}} \simeq 0.1 \text{ hMpc}^{-1}$), comparing the columns labeled as ‘‘w/o offset’’ and ‘‘with offset’’ shows that the lensing FoG correction improves the marginalized error of f_ν or w_0 by about 5-25% for BOSS, PFS or Euclid. However, as the power spectrum information up to the higher k_{max} is included, the bias due to the imperfect modeling of FoG effect becomes more significant, as shown in the rows denoted by ‘‘ $C = 0.7$ ’’. Thus even if the statistical precision is apparently improved in such high- k regime, a more accurate modeling of the FoG effect is needed in order not to have any significant parameter bias. For BOSS or PFS surveys, the amount of the bias on f_ν or w_0 is still smaller than the (marginalized) statistical error, while the bias becomes significant for Euclid survey. Finally we remark on the results that directions in the parameter bias are opposite for the results with and without the lensing priors on the off-centering parameters. For example, for a Gaussian FoG model case, we have found that, if including the lensing prior on the FoG suppression scale (i.e. the case with ‘‘with offset’’), the model prediction tends to overestimate the FoG suppression as implied in Fig. 8, and thus prefers a smaller f_ν , i.e. $\delta f_\nu < 0$. On the other hand, if the FoG suppression scale is treated as a free parameter (i.e. the case ‘‘w/o offset’’), the fitting tends to prefer a smaller FoG suppression, and in turn prefer a larger neutrino mass (larger f_ν); $\delta f_\nu > 0$.

The Gaussian and Lorentzian approximations are not sufficiently accurate to fully describe the FoG shape at $k \gtrsim 0.15 \text{ h/Mpc}$. Fig. 11 shows the systematic impact on the marginalized errors of (f_ν, w_0) for BOSS and PFS surveys with different k_{max} values. In this Fisher analysis both f_ν and w_0 are treated as free parameters in the model fitting (the growth rate $f_g(z_i)$ is fixed to the fiducial value). The error ellipse in each panel shows that the parameter w_0 and f_ν are correlated with each other in the measured DLRG power spectrum. The figure

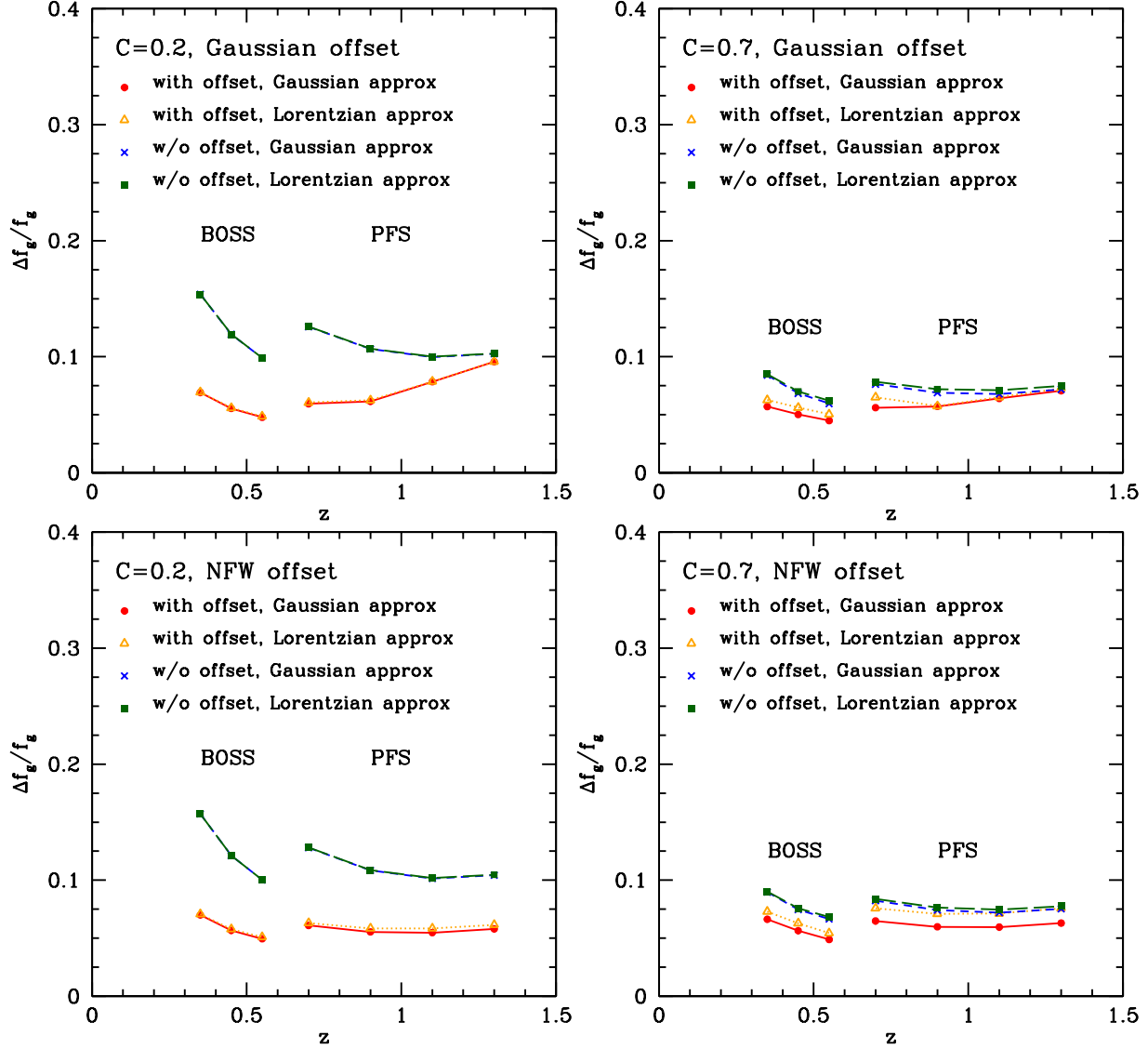


Figure 9. The marginalized error on the growth rate $f_g (\equiv d \ln D / d \ln a)$ at each redshift slices of BOSS and PFS surveys, expected when either of the two surveys is combined with the Planck CMB information. Note that the error shown here includes both the statistical and systematic error contributions (see Eq. [34]). The left- and right-side panels differ in the maximum wavenumber k_{\max} that is determined by the criterion of either $C = 0.2$ or 0.7 , respectively (see Eqs. [30] and [26] and Table 1). For the upper- and lower-side panels, we assume Gaussian and NFW radial profiles of DLRGs respectively, as in Fig. 2. The long- and short-dashed curves show the results when the FoG effect is modeled by either Gaussian or Lorentzian form and the model parameter $\sigma_{v,\text{off}}$ (Eq. [28]) is treated as a free parameter in the model fitting. The solid and dotted curves show the results including the DLRG-galaxy weak lensing information on $\sigma_{v,\text{off}}$ in Table 2. An inaccuracy of the approximated FoG form biases the growth rate estimation more significantly when including up to the higher k 's, as implied in the right-side panels.

shows that an imperfect modeling of the FoG effect may bias the parameters. However, the amount of the bias is still at $1\text{-}\sigma$ confidence level in the two-dimensional space for these surveys.

Fig. 12 shows the forecasts for the combined experiments of Planck CMB combined with BOSS, PFS and HSC (upper panels) and Planck CMB with Euclid (lower), respectively. The figure shows that the error ellipses are further shrunk by having the power spectrum information over a wider range of redshifts. As a result, the marginalized errors of $\sigma(f_\nu) \simeq 0.011(0.009)$ [or equivalently $\sigma(m_{\nu,\text{tot}}) \simeq 0.11(0.093)$ eV] and $\sigma(w_0) \simeq 0.063(0.051)$ can be achieved at $C = 0.2(0.7)$ for the BOSS+PFS+HSC survey. In Euclid survey, the error decreases to $\sigma(f_\nu) \simeq 0.0035(0.0028)$ [$\sigma(m_{\nu,\text{tot}}) = 0.035(0.028)$ eV] and $\sigma(w_0) \simeq 0.029(0.024)$ at $C = 0.2(0.7)$. In particular the Euclid survey allows for a detection of the non-zero neutrino masses at more than 1σ significance, because the lower mass bound for the normal or inverted mass hierarchy is about 0.05 or 0.1 eV, respectively. Thus such a high-precision determination of these parameters is potentially feasible for these surveys *if* we can use a sufficiently accurate model of the FoG in order to include the power spectrum amplitude information up to such higher k 's.

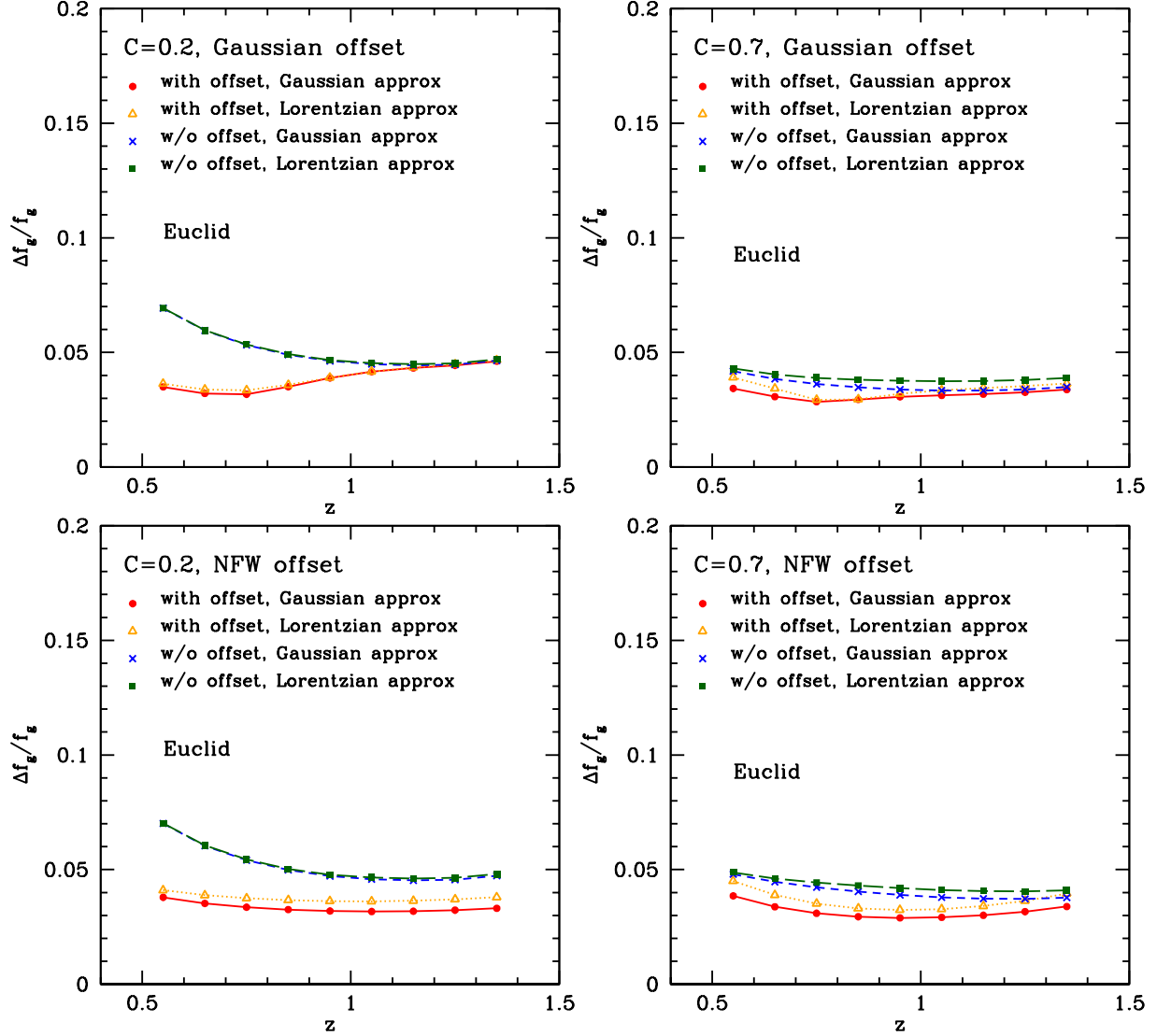


Figure 10. Similar to Fig 9, but for the Euclid survey.

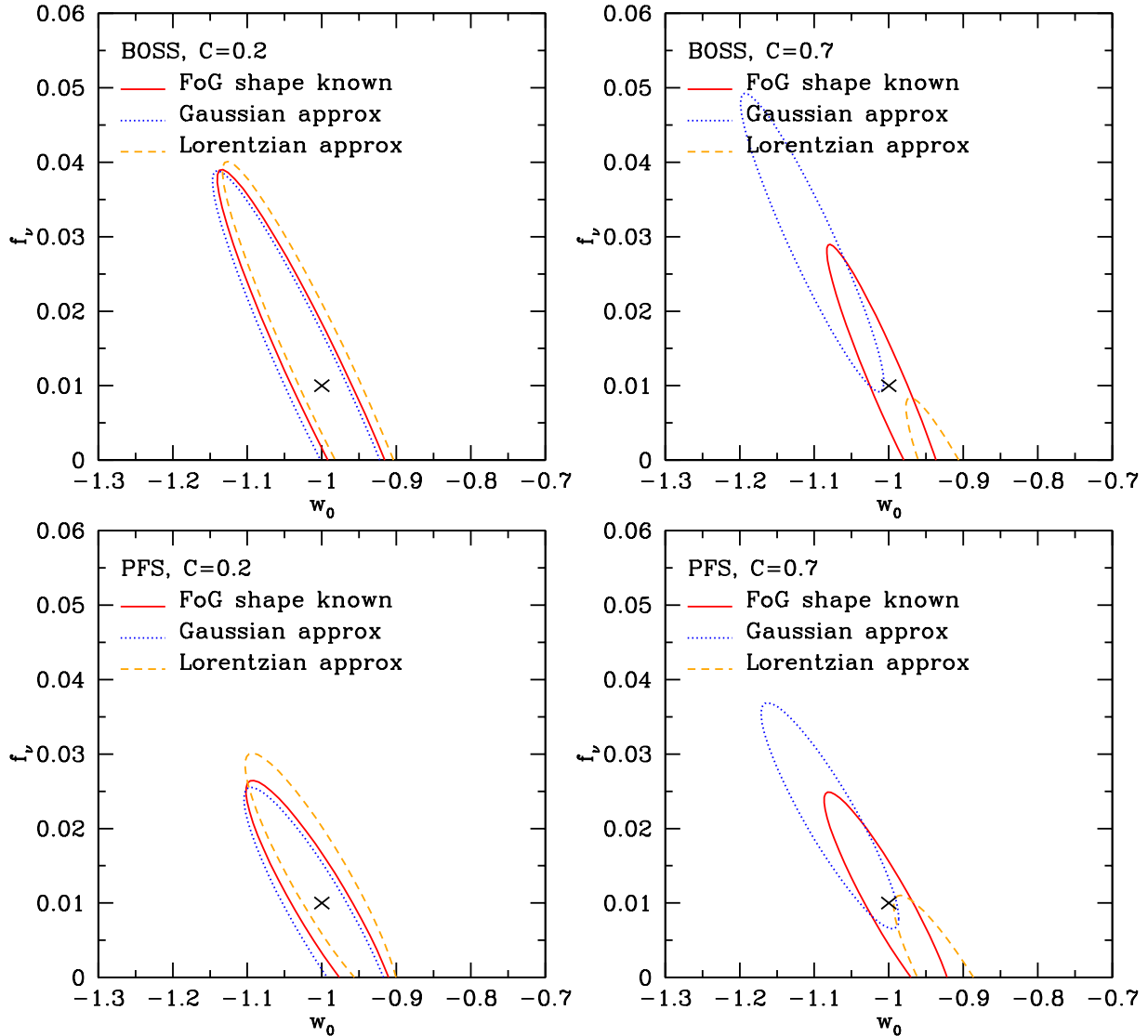
 Marginalized Error and Bias of Neutrino Mass (f_ν)

Survey	k_{\max}	w/o offset			with offset			FoG shape known	FoG neglected
		$\sigma(f_\nu)$	$\delta f_\nu(\text{Gauss})$	$\delta f_\nu(\text{Lorentz})$	$\sigma(f_\nu)$	$\delta f_\nu(\text{Gauss})$	$\delta f_\nu(\text{Lorentz})$	$\sigma(f_\nu)$	δf_ν
BOSS	C=0.2	0.0080	0.0001	-0.0002	0.0058(27%)	-0.0009	0.0014	0.0063	0.03
	C=0.7	0.0052	0.0022	-0.0027	0.0046(12%)	-0.0022	0.0031	0.0050	0.08
PFS	C=0.2	0.0068	0.0004	-0.0007	0.0057(16%)	-0.0006	0.0010	0.0063	0.04
	C=0.7	0.0051	0.0022	-0.0032	0.0049(4%)	0.0003	-0.0003	0.0051	0.08
EUCLID	C=0.2	0.0025	0.0005	-0.0010	0.0023(9%)	-0.0002	0.0003	0.0024	0.04
	C=0.7	0.0020	0.0025	-0.0035	0.0020(1%)	0.0017	-0.0025	0.0020	0.07

Table 3. Marginalized error and bias of f_ν for either BOSS, PFS, or Euclid survey combined with the Planck CMB information. Here we assume the FoG effect due to our fiducial Gaussian DLRG radial profile model, as in Fig. 9, and assume $f_\nu = 0.01$ ($m_{\nu, \text{tot}} = 0.104$ eV) as the fiducial values. Each column shows the statistical error ($\sigma(f_\nu)$) and the amount of bias ($\delta f_\nu \equiv f_{\nu, \text{est}} - f_{\nu, \text{true}}$) due to the difference of the assumed Gaussian (Gauss) or Lorentzian (Lorentz) FoG model from the input FoG effect that is computed based on our halo model. The columns labeled as “with offset” and “w/o offset” show the results with and without the lensing information being used to correct the FoG effect. The percentage numbers in parentheses in the $\sigma(f_\nu)$ column denote an improvement in the errors due to the lensing information. The column “FoG shape known” shows the statistical error when the same lensing information is added but assuming the shape of the FoG effect is known based on the halo model (see text for details). The column “FoG neglected” shows the parameter bias where the FoG effect is completely ignored (i.e. $\bar{\sigma}_{\nu, \text{off}} = 0$ is set). These results show a significant bias, more than 100% bias compared to the input value $f_\nu = 0.01$.

Marginalized Error and Bias of w_0

Survey	k_{\max}	w/o offset			with offset			FoG shape known	FoG neglected
		$\sigma(w_0)$	$\delta w_0(\text{Gauss})$	$\delta w_0(\text{Lorentz})$	$\sigma(w_0)$	$\delta w_0(\text{Gauss})$	$\delta w_0(\text{Lorentz})$	$\sigma(w_0)$	δw_0
BOSS	C=0.2	0.038	0.000	0.000	0.029(23%)	-0.004	0.007	0.031	0.15
	C=0.7	0.027	0.007	-0.009	0.021(20%)	-0.018	0.024	0.024	0.41
PFS	C=0.2	0.039	0.001	-0.001	0.034(13%)	-0.004	0.007	0.037	0.20
	C=0.7	0.032	0.007	-0.009	0.030(9%)	-0.009	0.015	0.032	0.53
EUCLID	C=0.2	0.017	0.003	-0.005	0.014(17%)	-0.003	0.006	0.016	0.25
	C=0.7	0.014	0.016	-0.022	0.013(5%)	0.004	-0.004	0.014	0.64

Table 4. Similar to Table 3, but for the dark energy equation-of-state parameter w_0 . Note that for these results the neutrino mass is fixed to the fiducial value $f_\nu = 0$.**Figure 11.** The marginalized error ellipses in a sub-space of (w_0, f_ν) , where both the parameters are included in the Fisher analysis. Solid ellipse represents the error when the FoG shape is completely known (i.e. “FoG shape known”), while the other ellipses show the errors when the FoG effect is approximated with Gaussian or Lorentzian forms “with offset” (dotted and dashed respectively). The imperfect modeling of the FoG effect biases the results different from the input values denoted by cross symbols. The lensing information is added for all plots. The different panels differ in the hypothetical spectroscopic survey (BOSS or PFS) and the maximum wavenumber k_{\max} used in the Fisher analysis ($C = 0.2$ or 0.7).

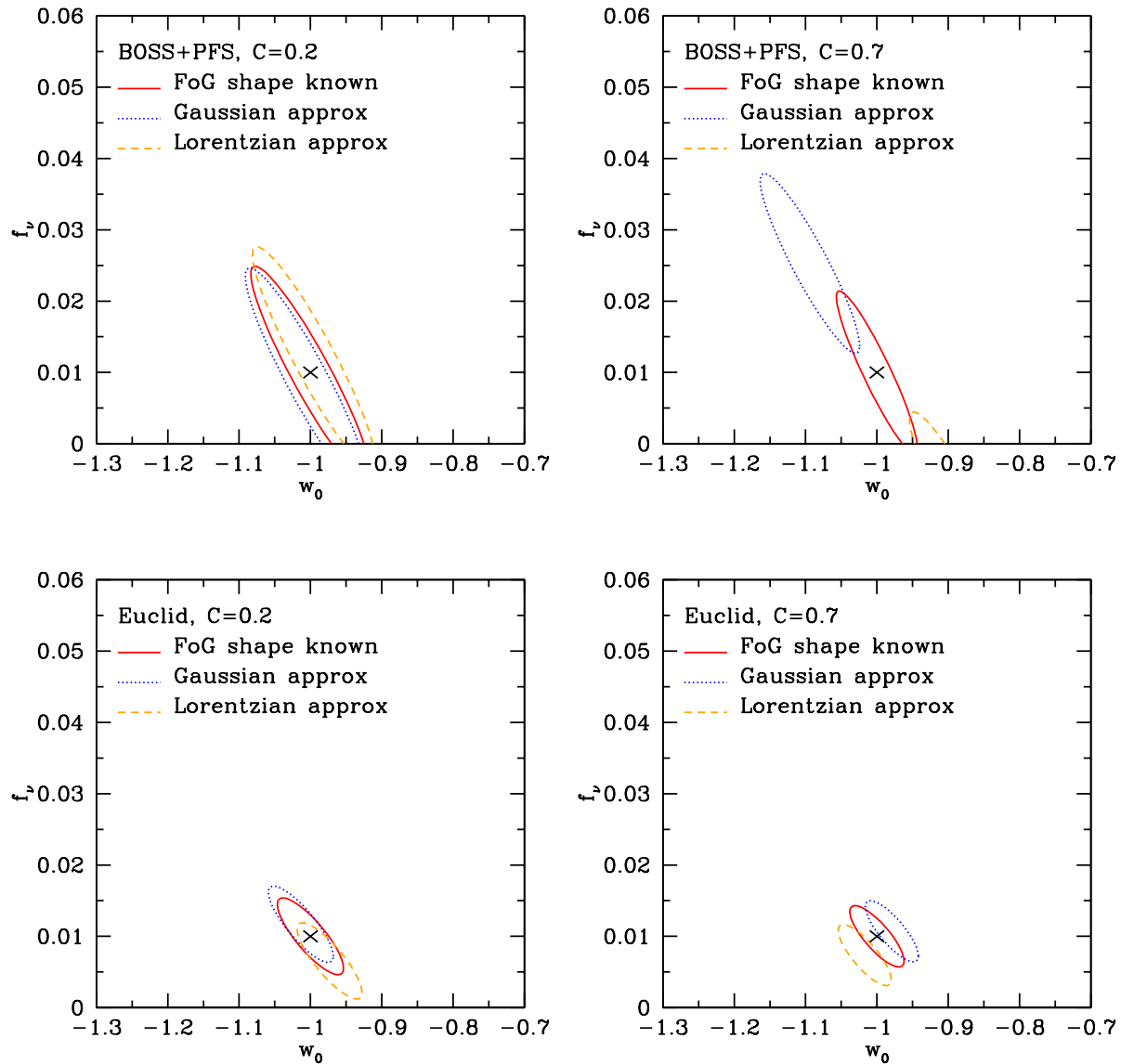


Figure 12. Similar to the previous figure, but for the joint experiments of HSC+BOSS+PFS+Planck (*upper panels*) and Euclid+Planck (*lower*).

5 SUMMARY AND DISCUSSION

Our lack of understanding of the relationship between the positions of galaxies in redshift space and the underlying distribution of matter is the largest systematic source of errors in the analysis of redshift surveys. If the dominant galaxy (e.g., the brightest cluster galaxy) in each halo was at rest in the center of the halo, then there would be minimal Finger-of-God (FoG) effects in a properly selected sample, nor any suppression of the power spectrum amplitude due to finite size of galaxy halos. We have quantified the deviations from this simple universe in terms of galaxy radial distribution, the probability of finding a galaxy at a given distance from the center of the halo. Since galaxies not in the centers of the gravitational potential are moving relative to the potential, thus the amplitude of this displacement is directly related to the amplitude of the FoG effect.

In this paper, we have showed how galaxy-galaxy lensing observations, which measure the relationship between galaxy positions and the distribution of dark matter in a statistical sense, can be used to measure this profile and reduce the uncertainties in analyses of galaxy power spectrum measurements. We have studied a case of luminous red galaxies (LRG), especially the dominant LRG in each halo (DLRG), as a working example for demonstrating an expected performance of our proposing method. We have assumed DLRG off-centered profiles motivated by the weak lensing study (Oguri et al. 2010) and the analysis (Ho et al. 2009) studying offsets of LRGs relative to the peak in X-ray brightness. Our DLRG radial profile model predicts that the FoG effect suppresses the DLRG power spectrum amplitudes at $k \sim 0.1$ and $0.2h/\text{Mpc}$ by 10 and 30%, respectively, much greater than the statistical precision of power spectrum measurements for ongoing and

upcoming spectroscopic surveys (see Fig. 8). The halos with masses $\sim 10^{14} M_{\odot}$ make the dominant contribution to the FoG effect on the DLRG power spectrum.

If we can measure the radial distribution, then we can model this effect and remove (or at least significantly reduce) this source of systematic uncertainty. We have illustrated this correction for ongoing and upcoming surveys: the BOSS survey, the Subaru imaging (HSC) and spectroscopic (PFS) surveys and ESA's Euclid mission (see Table 1). For example, the Subaru HSC imaging survey covering an area of 2000 square degrees can accurately measure the DLRG-galaxy lensing profile down to scales of an arcminute enabling an accurate characterization of the DLRG off-centered profile (see Fig. 6 and Table 2). As we have showed, this radial distribution can be used to correct the FoG effect and significantly improve parameter estimation from the redshift-space power spectrum measurements. We have illustrated this effect by discussing the impact of FoG effect on the parameters w_0 and f_{ν} as well as the growth rate $f_g \equiv d \ln D / d \ln a$ at each redshift slice. We have found that combining the lensing measurements with the redshift-space power spectrum can improve the constraints on f_g up to a factor of 2, compared to the case that the FoG effect is considered unknown, if the power spectrum information down to $k_{\max} \simeq 0.1$ or $0.2 h/\text{Mpc}$ is included (see Fig. 9). Including the lensing correction also improves measurements of w_0 and f_{ν} by 5-25%. Such a factor of 2 improvement in the parameter corresponds to a factor of 4 larger survey volume, and therefore the combined imaging and spectroscopic surveys can bring a huge beneficial synergy.

The analyses in this paper have made a number of simplifying assumptions that would have to be improved in a realistic analysis of a large spectroscopic survey. We have assumed a linear model for redshift distortion effect on halo power spectrum (the Kaiser formulation in Eq. [9]). The quality of the rapidly improving redshift data requires more refined model based on extended perturbation theory as well as simulations (Scoccimarro 2004; Taruya et al. 2010; Tang et al. 2011; Sato & Matsubara 2011). We have also assumed a linear bias model. Saito et al. (2011) found that non-linear bias corrections are important for the SDSS DLRGs.

In this paper, for simplicity, we have assumed that the velocity dispersion of DLRGs is determined by an enclosed mass (mostly dark matter) at a given radius and that the velocity distribution of DLRGs obeys a Gaussian distribution in a statistical average sense (see Eqs. [14] and [17]). However, the velocity distribution should be by nature sensitive to various complicated physics and galaxy formation physics, so it is still difficult to understand based on theoretical studies. Therefore an observational approach to tackling this issue is rather more adequate. For example, one may be able to use spectroscopic redshifts of galaxies, from a survey data itself or from a dedicated survey with optimized fiber positioning, to explore the velocity structures of DLRGs around massive halos based on the stacking analysis (Becker et al. 2007; White et al. 2010; Skibba et al. 2011) (also see Lam et al. in preparation). Or an alternative approach on the analysis side is to use an empirical model of the FoG effect which is given by a multiplicative function of the Gaussian FoG form and a perturbative functional form $[1 + a_0(k\mu)^2 + a_1(k\mu)^4 + \dots]$, where the coefficients a_0, a_1 are treated as nuisance parameters. The model defined in this way can have more degrees of freedom to describe possible complicated scale-dependences in genuine FoG effects (Tang et al. 2011, for a similar approach). Then, by using the generalized FoG form, we may be able to derive more robust, unbiased cosmological constraints including marginalization over the nuisance parameters, but still using the lensing information of off-centered DLRGs to constrain the Gaussian FoG part as we did in this paper.

There is more work needed to explore the effects of DLRG offsets on galaxy power spectra and lensing. Since galaxies of a given type lies in a range of halo masses, it is important to trace the dependence of the DLRG clustering and the FoG effect on halo mass scale: for the clustering, halos with typical mass scale of $\sim 10^{13} M_{\odot}$ gives a dominant contribution, while the FoG effect arises mainly from more massive halos with masses around $10^{14} M_{\odot}$. It would be useful to select a sample of massive halos focused on the high mass range to more accurately explore the offset of the DLRG from the halo centers as defined by optical, X-ray and SZ data. In this approach, weak lensing can play an important role, as various halo center indicators can be used to monitor weak lensing signals at small angular scales in both individual cluster lensing and stacked analysis bases (Johnston et al. 2007; Leauthaud et al. 2010; Okabe et al. 2010; Oguri et al. 2010; Oguri & Takada 2011).

Besides the cosmological use, the off-centering information of DLRGs should be very useful to develop a more physical understanding of the dynamical processes of DLRGs within the main halo. DLRGs are likely to reside on one of the most massive sub-halos within the main host halo with $\gtrsim 10^{13} M_{\odot}$. Therefore DLRG within each halo tends to sink towards the halo center due to dynamical friction, which is one of basic explanations for a more centrally concentrated distribution of DLRGs within halos compared to the dark matter distribution. The dynamical processes and assembly histories of DLRGs, within a given time scale of cluster-scale halos, are a key information to understanding the nature of DLRGs in the context of CDM dominated structure formation scenario. Again the galaxy-galaxy lensing can offer a new method of tackling these issues.

ACKNOWLEDGMENTS

We thank Joanne Cohn, Daniel Eisenstein, Issha Kayo, Eiichiro Komatsu, Rachel Mandelbaum, Nikhil Padmanabhan, John Peacock, Beth Reid and Martin White for useful discussion and valuable comments. CH acknowledges support from a Japan Society for Promotion of Science (JSPS) fellowship. MT thanks Department of Astrophysical Sciences, Princeton University for its warm hospitality during his visit, where this work was initiated. DNS and CH acknowledge support from NSF grant AST-0707731 and the NASA AST theory program. DNS thanks the IPMU for its warm hospitality during his visit, where the work was completed. This work is in part supported in part by JSPS Core-to-Core Program "International Research Network for Dark Energy", by Grant-in-Aid for Scientific Research from the JSPS Promotion

of Science, by Grant-in-Aid for Scientific Research on Priority Areas No. 467 “Probing the Dark Energy through an Extremely Wide & Deep Survey with Subaru Telescope”, by World Premier International Research Center Initiative (WPI Initiative), MEXT, Japan, and by the FIRST program “Subaru Measurements of Images and Redshifts (SuMIRe)”, CSTP, Japan.

REFERENCES

- Albrecht A., Bernstein G., Cahn R., Freedman W. L., Hewitt J., Hu W., Huth J., Kamionkowski M., Kolb E. W., Knox L., Mather J. C., Stags S., Suntzeff N. B., 2006, ArXiv Astrophysics e-prints
- Alcock C., Paczynski B., 1979, *Nature*, 281, 358
- Becker M. R., McKay T. A., Koester B., Wechsler R. H., Rozo E., Evrard A., Johnston D., Sheldon E., Annis J., Lau E., Nichol R., Miller C., 2007, *ApJ*, 669, 905
- Binney J., Tremaine S., 2008, *Galactic Dynamics: Second Edition*, Binney, J. & Tremaine, S., ed. Princeton University Press
- Blake C., Brough S., Colless M., Contreras C., Couch W., Croom S., Davis T., Drinkwater M. J., Forster K., Gilbank D., Gladders M., Glazebrook K., Jelliffe B., Jurek R. J., Li I.-H., Madore B., Martin D. C., Pimblett K., Poole G. B., Pracy M., Sharp R., Wisnioski E., Woods D., Wyder T. K., Yee H. K. C., 2011, *mnras*, 415, 2876
- Cole S., et al., 2005, *ApJ*, 362, 505
- Cooray A., Sheth R., 2002, *Physics Report*, 372, 1
- Crocce M., Scoccimarro R., 2006, *Phys. Rev. D*, 73, 063519
- Davis M., Huchra J., 1982, *ApJ*, 254, 437
- de Lapparent V., Geller M. J., Huchra J. P., 1986, *ApJ*, 302, L1
- de Putter R., Takada M., 2010, *prd*, 82, 103522
- Duffy A. R., Schaye J., Kay S. T., Dalla Vecchia C., 2008, *MNRAS*, 390, L64
- Eisenstein D. J., Hu W., Tegmark M., 1999, *ApJ*, 518, 2
- Eisenstein D. J., et al., 2001, *AJ*, 122, 2267
- , 2005, *ApJ*, 633, 560
- Guzik J., Jain B., Takada M., 2010, *Phys. Rev. D*, 81, 023503
- Guzzo L., et al., 2008, *Nature*, 451, 541
- Hamilton A. J. S., 1998, in *Astrophysics and Space Science Library*, Vol. 231, *The Evolving Universe*, D. Hamilton, ed., pp. 185–+
- Hilbert S., White S. D. M., 2010, *MNRAS*, 404, 486
- Ho S., Lin Y., Spergel D., Hirata C. M., 2009, *ApJ*, 697, 1358
- Jackson J. C., 1972, *MNRAS*, 156, 1P
- Johnston D. E., et al., 2007, ArXiv e-prints
- Kaiser N., 1987, *MNRAS*, 227, 1
- Kirshner R. P., Oemler Jr. A., Schechter P. L., Sheckman S. A., 1987, *ApJ*, 314, 493
- Koester B. P., et al., 2007, *ApJ*, 660, 239
- Komatsu E., et al., 2009, *Astropys.J.Suppl.*, 180, 330
- Leauthaud A., et al., 2010, *ApJ*, 709, 97
- Lewis A., Challinor A., Lasenby A., 2000, *ApJ*, 538, 473
- Limber D. N., 1954, *ApJ*, 119, 655
- Lin Y., Mohr J. J., 2004, *ApJ*, 617, 879
- LSST Science Collaborations, Abell P. A., et al., 2009, ArXiv e-prints
- Mandelbaum R., Seljak U., Kauffmann G., Hirata C. M., Brinkmann J., 2006, *MNRAS*, 368, 715
- Matsubara T., 2008, *Phys. Rev. D*, 78, 083519
- Miyazaki S., Komiyama Y., Nakaya H., Doi Y., Furusawa H., Gillingham P., Kamata Y., Takeshi K., Nariai K., 2006, in *Society of Photo-Optical Instrumentation Engineers (SPIE) Conference Series*, Vol. 6269, *Society of Photo-Optical Instrumentation Engineers (SPIE) Conference Series*
- Nakamura T. T., Suto Y., 1997, *Progress of Theoretical Physics*, 97, 49
- Nishizawa A. J., Takada M., Hamana T., Furusawa H., 2010, *ApJ*, 718, 1252
- Oguri M., Takada M., 2011, *Phys. Rev. D*, 83, 023008
- Oguri M., Takada M., Okabe N., Smith G. P., 2010, *MNRAS*, 405, 2215
- Okabe N., Takada M., Umetsu K., Futamase T., Smith G. P., 2010, *Publ. Soc. Astron. Japan*, 62, 811
- Okumura T., Matsubara T., Eisenstein D. J., Kayo I., Hikage C., Szalay A. S., Schneider D. P., 2008, *ApJ*, 676, 889
- Peacock J. A., Schneider P., Efstathiou G., Ellis J. R., Leibundgut B., Lilly S. J., Mellier Y., 2006, *ESA-ESO Working Group on “Fundamental Cosmology”*. Tech. rep.
- Peacock J. A., et al., 2001, *Nature*, 410, 169
- Percival W. J., Reid B. A., Eisenstein D. J., Bahcall N. A., Budavari T., Frieman J. A., Fukugita M., Gunn J. E., Ivezić Ž., Knapp G. R.,

- Kron R. G., Loveday J., Lupton R. H., McKay T. A., Meiksin A., Nichol R. C., Pope A. C., Schlegel D. J., Schneider D. P., Spergel D. N., Stoughton C., Strauss M. A., Szalay A. S., Tegmark M., Vogeley M. S., Weinberg D. H., York D. G., Zehavi I., 2010, *MNRAS*, 401, 2148
- Percival W. J., White M., 2009, *MNRAS*, 393, 297
- Percival W. J., et al., 2007, *ApJ*, 657, 51
- Reid B. A., Spergel D. N., 2009, *ApJ*, 698, 143
- Reid B. A., Spergel D. N., Bode P., 2009, *ApJ*, 702, 249
- Reid B. A., White M., 2011, *mnras*, 417, 1913
- Reid B. A., et al., 2010, *ApJ*, 404, 60
- Ross N. P., et al., 2007, *MNRAS*, 381, 573
- , 2008, *MNRAS*, 387, 1323
- Saito S., Takada M., Taruya A., 2011, *prd*, 83, 043529
- Sato M., Matsubara T., 2011, *prd*, 84, 043501
- Schlegel D. J., et al., 2009, *ArXiv e-prints*
- Scoccimarro R., 2004, *Phys. Rev. D*, 70, 083007
- Scoccimarro R., Sheth R. K., Hui L., Jain B., 2001, *ApJ*, 546, 20
- Seljak U., 2001, *MNRAS*, 325, 1359
- Seo H., Eisenstein D. J., 2003, *ApJ*, 598, 720
- Sheldon E. S., et al., 2009, *ApJ*, 703, 2217
- Sheth R., Tormen G., 1999, *MNRAS*, 308, 119
- Skibba R. A., van den Bosch F. C., Yang X., More S., Mo H., Fontanot F., 2011, *MNRAS*, 410, 417
- Smith R. E., Peacock J. A., Jenkins A., White S. D. M., Frenk C. S., Pearce F. R., Thomas P. A., Efstathiou G., Couchman H. M. P., 2003, *MNRAS*, 341, 1311
- Song Y., Kayo I., 2010, *MNRAS*, 407, 1123
- Song Y., Percival W. J., 2009, *JCAP*, 10, 4
- Takada M., Bridle S., 2007, *New Journal of Physics*, 9, 446
- Takada M., Jain B., 2003, *MNRAS*, 340, 580
- , 2009, *MNRAS*, 395, 2065
- Takada M., Komatsu E., Futamase T., 2006, *Phys. Rev. D*, 73, 083520
- Takahashi R., Yoshida N., Takada M., Matsubara T., Sugiyama N., Kayo I., Nishizawa A. J., Nishimichi T., Saito S., Taruya A., 2009, *ApJ*, 700, 479
- Tang J., Kayo I., Takada M., 2011, *mnras*, 416, 2291
- Taruya A., Nishimichi T., Saito S., 2010, *Phys. Rev. D*, 82, 063522
- Taruya A., Nishimichi T., Saito S., Hiramatsu T., 2009, *Phys. Rev. D*, 80, 123503
- Tegmark M., et al., 2004, *ApJ*, 606, 702
- Wake D. A., et al., 2008, *MNRAS*, 387, 1045
- Wang Y., 2008, *JCAP*, 5, 21
- Wang Y., Spergel D. N., Strauss M. A., 1999, *ApJ*, 510, 20
- White M., 2001, *MNRAS*, 321, 1
- White M., Cohn J. D., Smit R., 2010, *MNRAS*, 408, 1818
- White M., Song Y., Percival W. J., 2009, *MNRAS*, 397, 1348
- White M., et al., 2011, *ApJ*, 728, 126
- Yamamoto K., Nakamura G., Hütsi G., Narikawa T., Sato T., 2010, *Phys. Rev. D*, 81, 103517
- York D. G., et al., 2000, *Astron. J.*, 120, 1579
- Zhang P., Liguori M., Bean R., Dodelson S., 2007, *Physical Review Letters*, 99, 141302
- Zheng Z., Zehavi I., Eisenstein D. J., Weinberg D. H., Jing Y. P., 2009, *ApJ*, 707, 554
- Zheng Z., et al., 2005, *ApJ*, 633, 791

APPENDIX A: ISOTHERMAL VELOCITY DISPERSION MODEL

In this appendix, we show an alternative model of the velocity dispersion of DLRGs following the theory in Binney & Tremaine (2008), which differs from the model in Section 2.3.3.

Let us begin our discussion with assuming that the phase space density of DLRGs, which reside in host halo of mass M , obeys an isothermal distribution (Eq. [4-116] in Binney & Tremaine (2008)):

$$f(r, \mathbf{v}; M) = \frac{\rho_1}{(2\pi\sigma_{\text{DLRG}}^2(r; M))^{3/2}} \exp\left(\frac{\Psi(r) - |\mathbf{v}|^2/2}{\sigma_{v,\text{iso}}^2(r; M)}\right) \quad (\text{A1})$$

where $\Psi(r)$ is the gravitational potential determined by dark matter distribution, $\sigma_{v,\text{iso}}^2(r; M)$ is the 1D velocity dispersion of DLRGs and ρ_1 is the normalization constant. Here we assume a spherically symmetric distribution for the DLRG distribution in a statistical average sense. Although DLRGs obey such an isothermal distribution in the potential well of dark matter, this is an alternative model to estimate the DLRG velocity dispersion, so let us continue our discussion.

Integrating the equation above over velocities yields the radial profile of DLRGs, which should be equivalent to the off-centered profile in our language:

$$p_{\text{off}}(r; M) = \rho_1 \exp\left(\frac{\Psi(r)}{\sigma_{v,\text{iso}}^2(r; M)}\right). \quad (\text{A2})$$

This equation gives us an inverse problem: once the off-centered profile and the gravitational potential are given, the velocity dispersion $\sigma_{v,\text{iso}}$ is determined.

Assuming an NFW profile for the total mass profile within the halo, the gravitational potential is given via Poisson's equation as

$$\frac{1}{r^2} \frac{d}{dr} \left(r^2 \frac{d\Psi(r)}{dr} \right) = -4\pi G \rho_{\text{DM}}(r), \quad (\text{A3})$$

Hence the potential is given as

$$\begin{aligned} \Psi(r) &= - \int_0^r dr' \frac{GM(<r')}{r'^2}, \\ &= 2\sigma_v^2(r; M) \frac{I(r/r_s)}{m_{\text{nfw}}(c)/c}, \end{aligned} \quad (\text{A4})$$

with

$$\begin{aligned} m_{\text{nfw}}(x) &\equiv \ln(1+x) - \frac{x}{1+x}, \\ I(x) &\equiv \int_0^x dx' \frac{m_{\text{nfw}}(x')}{x'^2} = 1 - \frac{\ln(1+x)}{x}. \end{aligned} \quad (\text{A5})$$

Here we have rewritten the equation above in terms of the virial velocity dispersion $\sigma_v(r; M)$ defined in Eq. (14).

Inserting Eq. (A4) into Eq. (A2) yields

$$p_{\text{off}}(r; M) = \rho_1 \exp\left(-\frac{2\sigma_v^2(r; M)}{\sigma_{v,\text{iso}}^2(r; M)} \frac{I(r/r_s)}{m_{\text{nfw}}(c)/c}\right). \quad (\text{A6})$$

The normalization constant ρ_1 is determined by imposing that the velocity dispersion $\sigma_{v,\text{iso}}$ is the same as σ_v at the limit $r \rightarrow 0$:

$$\begin{aligned} \rho_1 &= p_{\text{off}}(r_{\text{piv}}) \exp\left(\frac{2I(r_{\text{piv}}/r_s)}{m(r_{\text{piv}}/r_s)/r_{\text{piv}}/r_s}\right) \\ &\simeq p_{\text{off}}(r_{\text{piv}}) \exp(2) \quad (r_{\text{piv}}/r_s \ll 1) \end{aligned} \quad (\text{A7})$$

where r_{piv} is a pivot radius we choose to impose the conditions that r_{piv} is very small as well as $\sigma_{v,\text{iso}} = \sigma_v$ at $r = r_{\text{piv}}$. Hence, the velocity dispersion for an isothermal distribution model can be given in terms of the off-centered profile as

$$\sigma_{v,\text{iso}}^2(r; M) = \sigma_{\text{vir}}^2(M) \frac{I(r/r_s)}{m_{\text{nfw}}(c)/c} \left[1 - \frac{1}{2} \ln\left(\frac{p_{\text{off}}(r; M)}{p_{\text{off}}(r_{\text{piv}}; M)}\right) \right]^{-1}. \quad (\text{A8})$$

Fig. A1 shows the velocity dispersion for this isothermal distribution model, comparing with our fiducial model based on a simple virial theorem (Eq. [14]). To compute this velocity profile, we use $r_{\text{piv}}/r_s = 10^{-4}$. However note that the dependence of r_{piv} is small because the dependence is logarithmic as implied in Eq. (A8). The figure shows that the isothermal model gives a smaller velocity dispersion than the fiducial model, and therefore the resulting FoG effect is smaller than the results shown in the main text, by about factor of 2 in the power spectrum amplitudes.

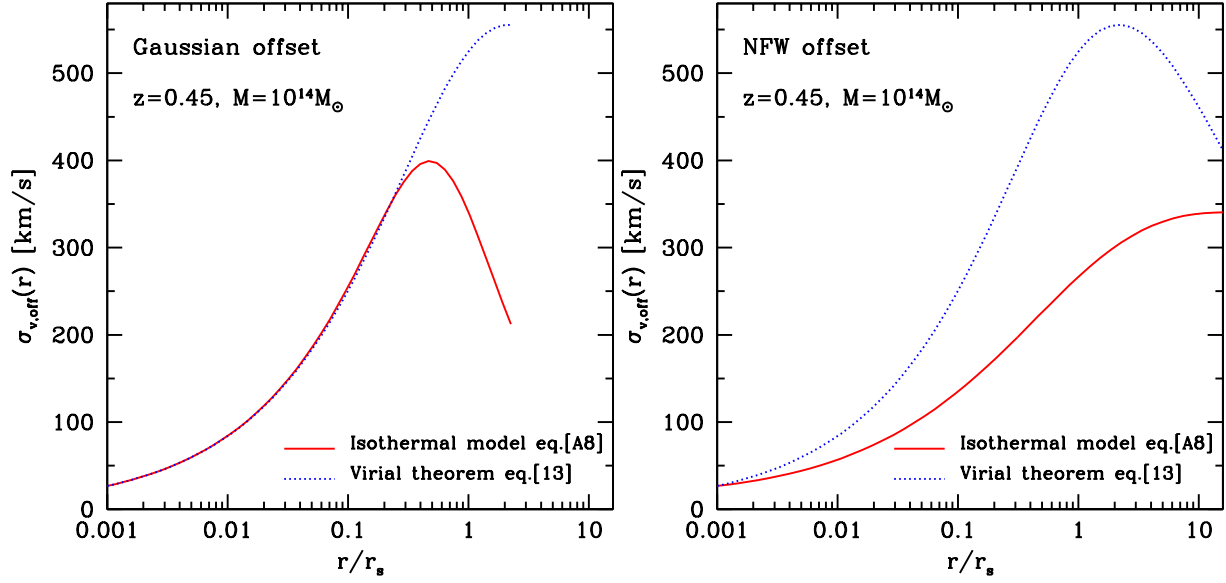


Figure A1. Comparing the models of DLRG velocity dispersion within a halo with $10^{14} M_{\odot}$ and at redshift $z = 0.45$. The two models to be compared are a model based on the virial theorem (Eq. [14]) and a model derived assuming an isothermal velocity distribution given the off-centered profile of DLRGs and the dark matter mass profile. The left- and right panels show the results assuming the Gaussian and NFW off-centered profiles, respectively. The model given in Appendix A gives a smaller velocity dispersion than our fiducial model.